

Exploring $N_f = 2 + 1$ QCD thermodynamics from the gradient flow

Yusuke Taniguchi,^{1,*} Shinji Ejiri,^{2,†} Ryo Iwami,^{3,‡} Kazuyuki Kanaya,^{4,§} Masakiyo Kitazawa,^{5,6,¶} Hiroshi Suzuki,^{7,**} Takashi Umeda,^{8,††} and Naoki Wakabayashi^{3,‡‡}

(WHOT-QCD Collaboration)

¹*Center for Computational Sciences (CCS),
University of Tsukuba, Tsukuba, Ibaraki 305-8571, Japan*

²*Department of Physics, Niigata University, Niigata 950-2181, Japan*

³*Graduate School of Science and Technology,
Niigata University, Niigata 950-2181, Japan*

⁴*Center for Integrated Research in Fundamental Science and Engineering (CiRfSE),
University of Tsukuba, Tsukuba, Ibaraki 305-8571, Japan*

⁵*Department of Physics, Osaka University, Osaka 560-0043, Japan*

⁶*J-PARC Branch, KEK Theory Center,
Institute of Particle and Nuclear Studies, KEK,
203-1, Shirakata, Tokai, Ibaraki, 319-1106, Japan*

⁷*Department of Physics, Kyushu University,
744 Motoooka, Fukuoka 819-0395, Japan*

⁸*Graduate School of Education, Hiroshima University,
Higashihiroshima, Hiroshima 739-8524, Japan*

(Dated: February 21, 2019)

Abstract

The energy-momentum tensor plays an important role in QCD thermodynamics. Its expectation value contains information of the pressure and the energy density as its diagonal part. Further properties like viscosity and specific heat can be extracted from its correlation function. A non-perturbative evaluation of it on the lattice is called. Recently a new method based on the gradient flow was introduced to calculate the energy-momentum tensor on the lattice, and has been successfully applied to quenched QCD. In this paper, we apply the gradient flow method to calculate the energy-momentum tensor in $(2 + 1)$ -flavor QCD adopting a nonperturbatively $O(a)$ -improved Wilson quark action and the renormalization group-improved Iwasaki gauge action. As the first application of the method with dynamical quarks, we study at a single but fine lattice spacing $a \simeq 0.07$ fm with heavy u and d quarks ($m_\pi/m_\rho \simeq 0.63$) and approximately physical s quark ($m_{\eta_{ss}}/m_\phi \simeq 0.74$). With the fixed-scale approach, temperature is varied by the temporal lattice size N_t at a fixed lattice spacing. Performing simulations on lattices with $N_t = 16$ to 4, the temperature range of $T \simeq 174$ – 697 MeV is covered. We find that the results of the pressure and the energy density by the gradient flow method are consistent with the previous results using the T -integration method at $T \lesssim 280$ MeV ($N_t \gtrsim 10$), while the results show disagreement at $T \gtrsim 350$ MeV ($N_t \lesssim 8$), presumably due to the small- N_t lattice artifact of $O((aT)^2) = O(1/N_t^2)$.

We also apply the gradient flow method to evaluate the chiral condensate taking advantage of the gradient flow method that renormalized quantities can be directly computed avoiding the difficulty of explicit chiral violation with lattice quarks. We compute the renormalized chiral condensate in the $\overline{\text{MS}}$ scheme at renormalization scale $\mu = 2$ GeV with a high precision to study the temperature dependence of the chiral condensate and its disconnected susceptibility. Even with the Wilson-type quark action which violates the chiral symmetry explicitly, we obtain the chiral condensate and its disconnected susceptibility showing a clear signal of pseudocritical temperature at $T \sim 190$ MeV related to the chiral restoration crossover.

* Corresponding author; tanigchi@het.ph.tsukuba.ac.jp

† ejiri@muse.sc.niigata-u.ac.jp

‡ iwami@muse.sc.niigata-u.ac.jp

§ kanaya@ccs.tsukuba.ac.jp

¶ kitazawa@phys.sci.osaka-u.ac.jp

** hsuzuki@phys.kyushu-u.ac.jp

†† tumeda@hiroshima-u.ac.jp

‡‡ wakabayashi@muse.sc.niigata-u.ac.jp

I. INTRODUCTION

Precise determination of thermodynamic properties of the quark matter is a key step towards understanding the early evolution of the Universe as well as the nature of neutron/quark stars. Numerical simulation of QCD on the lattice provides us with the only way to study the nature of the strongly coupled quark matter directly from the first principles of QCD. Recently, the Yang-Mills gradient flow [1–5] has introduced big advances in numerical determination of various observables in lattice QCD [6–8]. Fields at positive flow time, $t > 0$, can be viewed as smeared fields averaged over a mean physical radius of $\sqrt{8t}$ in four dimensions. Salient features of the gradient flow are the UV finiteness and the absence of short-distance singularities in the operators constructed by flowed fields at $t > 0$. This enables us to directly construct renormalized quantities in terms of the flowed fields, *i.e.*, a new renormalization scheme can be introduced by the gradient flow. Because the flowed fields are defined nonperturbatively, we can evaluate their nonperturbative expectation values directly on the lattice. This opened us a large variety of possibilities to significantly simplify the determination of physical observables on the lattice. In this paper, we determine the equation of state (EOS) as well as the chiral condensate in $(2 + 1)$ -flavor QCD at finite temperatures, by applying the methods of Refs. [9, 10] using the gradient flow. The EOS in $(2 + 1)$ -flavor QCD has been calculated at the physical point and extrapolated to the continuum limit using staggered-type lattice quarks [11, 12]. To avoid theoretical uncertainties with staggered-type lattice quarks, calculations using Wilson-type lattice quarks have been also attempted [13, 14]. See Ref. [15] for the recent status and related developments on the lattice.

In this study, we extract the EOS from the diagonal elements of the energy-momentum tensor, $T_{\mu\nu}(x)$. The energy-momentum tensor is the generator of continuous coordinate translations and thus, is not uniquely given on discrete lattices as a conserved current. An approach to overcome this problem is to use finite observables, which are independent of the regularization in the continuum limit. The gradient flow enables us to define such finite observables. Unfortunately these finite renormalized tensor operators are not necessarily equal to the conserved energy-momentum tensor but an appropriate combination of them can be the energy-momentum tensor in a small flow time limit [9, 16]. In Refs. [9, 16], coefficients needed to extract the energy-momentum tensor which satisfies the Ward-Takahashi identity

associated with the translational invariance from appropriate flowed tensor operators were calculated, by using a small flow time expansion of flowed operators [3]. In this method, we observe several lattice operators at small t and take their vanishing t limit. The coefficients relating these limiting values with the energy-momentum tensor is calculated in a renormalized theory. They can be computed by perturbation theory using the asymptotic freedom at small t , and those for the quenched case are computed in Ref. [16]. Finally, the EOS is given by $\epsilon = -\langle T_{00} \rangle$ and $p = \sum_i \langle T_{ii} \rangle / 3$, where ϵ and p are the energy density and the pressure, respectively. Some other thermodynamic quantities, such as the bulk and shear viscosities etc., can also be extracted from the energy-momentum tensor. Here, we stress that, though these coefficients are computed in perturbation theory, they are used just to guide the $t \rightarrow 0$ extrapolation. We thus consider that our evaluation of the energy-momentum tensor is essentially nonperturbative.¹

The method was tested in quenched QCD by the FlowQCD Collaboration in Ref. [19]. The resulting EOS from the gradient flow shows a good agreement with the previous results of the conventional integration and T -integration methods [13, 20–24].

In this paper, we extend the study of the energy-momentum tensor and EOS to QCD with dynamical quarks, adopting the method of Ref. [9]. The gradient flow in full QCD was investigated by Lüscher in Ref. [4]. Because the *raison d'être* of the gradient flow in our study is the semilocal smearing of the fields, it is not mandatory to introduce quarks in the dynamics of the flow in t . A numerically easier way is to keep the quenched flow equations for the gauge fields and combine them with a gauge-covariant quenched flow equation for the quark fields [4]. Fermionic operators, however, require additional wave function renormalization of quark fields, which can be carried out by normalizing the flowed quark fields by the vacuum expectation value of a flowed quark kinetic operator at zero temperature [9]. The coefficients required to compute the energy-momentum tensor and EOS in full QCD were computed in Ref. [9].

We note that the calculation of EOS by the gradient flow method does not require the information of beta functions. In a conventional calculation of EOS using the derivative method, the integration method, or T -integration method, evaluation of the nonperturbative beta functions is a big numerical task, in particular in full QCD for which we first have to determine a line of constant physics in a multidimensional coupling parameter space on

¹ This idea has been tested in solvable models [17, 18].

zero-temperature lattices and then measure the beta functions defined as the slopes of each coupling parameter under a variation of the lattice spacing a along the line of constant physics. With the fixed-scale approach using the T -integration method, the same set of zero-temperature configurations can be used to compute EOS at all temperatures, provided that the beta functions are available. If the beta functions are not available, we have to carry out a series of systematic zero-temperature simulations in a multidimensional parameter space to determine the beta functions, and thus the benefit of the fixed-scale approach is reduced. The gradient flow method in part removes the weak point of the fixed-scale approach.

In this study, we also calculate the chiral condensate. Using the gradient flow method of Ref. [10], the proper chiral condensate which satisfies the partially conserved axial vector current (PCAC) relation is extracted through a similar idea as the energy-momentum tensor.² The temperature dependence of the chiral condensate as well as its disconnected susceptibility is studied and a signal of chiral crossover is observed at $T \sim 190$ MeV.

The gradient flow method of Ref. [10] was also applied to study the topological susceptibility in finite temperature QCD [25]. Preliminary results of our study was reported in Refs. [26, 27]. This paper is organized as follows: In Sec. II, we define our gradient flow equations and give explicit formulas for the energy-momentum tensor and the chiral condensate. Our simulation parameters are summarized in Sec. III, and the results of the numerical simulation for the energy-momentum tensor and chiral condensate are presented in Secs. IV and V, respectively. Section VI is devoted to our conclusions and discussions. In Appendixes A and B, we introduce our simulation algorithms for the gradient flow and measurements with quarks. Definitions of our running coupling and running masses, which are necessary in the evaluation of conversion coefficients, are given in Appendix C. Several additional tests on our data for the energy-momentum tensor are presented in Appendix D.

² A different method to compute the chiral condensate by using the gradient flow has been discussed in Ref. [4].

II. DEFINITION OF OBSERVABLES

A. Flow equations

Our flow equations are identical to those given in Refs. [2] and [4]. That is, for the gauge field, we set³

$$\partial_t B_\mu(t, x) = D_\nu G_{\nu\mu}(t, x), \quad B_\mu(t = 0, x) = A_\mu(x), \quad (1)$$

where the field strength and the covariant derivative of the flowed gauge field are

$$G_{\mu\nu}(t, x) = \partial_\mu B_\nu(t, x) - \partial_\nu B_\mu(t, x) + [B_\mu(t, x), B_\nu(t, x)], \quad (2)$$

and

$$D_\nu G_{\nu\mu}(t, x) = \partial_\nu G_{\nu\mu}(t, x) + [B_\nu(t, x), G_{\nu\mu}(t, x)], \quad (3)$$

respectively. For the quark fields, we set

$$\partial_t \chi_f(t, x) = \Delta \chi_f(t, x), \quad \chi_f(t = 0, x) = \psi_f(x), \quad (4)$$

$$\partial_t \bar{\chi}_f(t, x) = \bar{\chi}_f(t, x) \overleftarrow{\Delta}, \quad \bar{\chi}_f(t = 0, x) = \bar{\psi}_f(x), \quad (5)$$

where $f = u, d, s$, denotes the flavor index, and

$$\Delta \chi_f(t, x) \equiv D_\mu D_\mu \chi_f(t, x), \quad D_\mu \chi_f(t, x) \equiv [\partial_\mu + B_\mu(t, x)] \chi_f(t, x), \quad (6)$$

$$\bar{\chi}_f(t, x) \overleftarrow{\Delta} \equiv \bar{\chi}_f(t, x) \overleftarrow{D}_\mu \overleftarrow{D}_\mu, \quad \bar{\chi}_f(t, x) \overleftarrow{D}_\mu \equiv \bar{\chi}_f(t, x) \left[\overleftarrow{\partial}_\mu - B_\mu(t, x) \right]. \quad (7)$$

Note that our flow equations are independent of the flavor.

B. Energy-momentum tensor

We follow the proposal of Refs. [9, 16, 19] which employs the gradient flow and the fermion flow and their small flow time expansion [3] to define the energy-momentum tensor. According to the reasoning of Refs. [9, 16], in terms of composite operators made out from

³ In what follows, the sum over repeated Lorentz indices, μ, ν, ρ, \dots , over 0, 1, 2, and 3, and the sum of the adjoint indices, a, b, \dots , are always understood. On the other hand, without indicated otherwise, the summation over repeated flavor indices, $f, f' = u, d, s$ is not assumed.

the flowed fields, the correctly normalized energy-momentum tensor is given by⁴

$$\begin{aligned}
T_{\mu\nu}(x) = \lim_{t \rightarrow 0} & \left\{ c_1(t) \left[\tilde{\mathcal{O}}_{1\mu\nu}(t, x) - \frac{1}{4} \tilde{\mathcal{O}}_{2\mu\nu}(t, x) \right] \right. \\
& + c_2(t) \left[\tilde{\mathcal{O}}_{2\mu\nu}(t, x) - \left\langle \tilde{\mathcal{O}}_{2\mu\nu}(t, x) \right\rangle_0 \right] \\
& + c_3(t) \sum_{f=u,d,s} \left[\tilde{\mathcal{O}}_{3\mu\nu}^f(t, x) - 2\tilde{\mathcal{O}}_{4\mu\nu}^f(t, x) - \left\langle \tilde{\mathcal{O}}_{3\mu\nu}^f(t, x) - 2\tilde{\mathcal{O}}_{4\mu\nu}^f(t, x) \right\rangle_0 \right] \\
& + c_4(t) \sum_{f=u,d,s} \left[\tilde{\mathcal{O}}_{4\mu\nu}^f(t, x) - \left\langle \tilde{\mathcal{O}}_{4\mu\nu}^f(t, x) \right\rangle_0 \right] \\
& \left. + \sum_{f=u,d,s} c_5^f(t) \left[\tilde{\mathcal{O}}_{5\mu\nu}^f(t, x) - \left\langle \tilde{\mathcal{O}}_{5\mu\nu}^f(t, x) \right\rangle_0 \right] \right\}, \tag{8}
\end{aligned}$$

where $\langle \dots \rangle_0$ stands for the vacuum expectation value (VEV), i.e., the expectation value at zero temperature. The operators in the right-hand side of Eq. (8) are defined by

$$\tilde{\mathcal{O}}_{1\mu\nu}(t, x) \equiv G_{\mu\rho}^a(t, x) G_{\nu\rho}^a(t, x), \tag{9}$$

$$\tilde{\mathcal{O}}_{2\mu\nu}(t, x) \equiv \delta_{\mu\nu} G_{\rho\sigma}^a(t, x) G_{\rho\sigma}^a(t, x), \tag{10}$$

$$\tilde{\mathcal{O}}_{3\mu\nu}^f(t, x) \equiv \varphi_f(t) \bar{\chi}_f(t, x) \left(\gamma_\mu \overleftrightarrow{D}_\nu + \gamma_\nu \overleftrightarrow{D}_\mu \right) \chi_f(t, x), \tag{11}$$

$$\tilde{\mathcal{O}}_{4\mu\nu}^f(t, x) \equiv \varphi_f(t) \delta_{\mu\nu} \bar{\chi}_f(t, x) \overleftrightarrow{D} \chi_f(t, x), \tag{12}$$

$$\tilde{\mathcal{O}}_{5\mu\nu}^f(t, x) \equiv \varphi_f(t) \delta_{\mu\nu} \bar{\chi}_f(t, x) \chi_f(t, x), \tag{13}$$

where

$$\overleftrightarrow{D}_\mu \equiv D_\mu - \overleftarrow{D}_\mu, \tag{14}$$

and for the $(2+1)$ -flavor QCD, the normalization factor $\varphi_f(t)$ is given by [9],

$$\varphi_f(t) \equiv -\frac{6}{(4\pi)^2 t^2 \left\langle \bar{\chi}_f(t, x) \overleftrightarrow{D} \chi_f(t, x) \right\rangle_0}. \tag{15}$$

Note that, from above definitions, it follows that

$$2 \left\langle \tilde{\mathcal{O}}_{3\mu\nu}^f(t, x) \right\rangle_0 = \left\langle \tilde{\mathcal{O}}_{4\mu\nu}^f(t, x) \right\rangle_0 = -\frac{6}{(4\pi)^2 t^2} \delta_{\mu\nu}. \tag{16}$$

⁴ In this definition, we subtract the vacuum expectation value of the operator which might be divergent.

The coefficients in Eq. (8) for $(2 + 1)$ -flavor QCD are given as [9],

$$c_1(t) = \frac{1}{\bar{g}(1/\sqrt{8t})^2} - \frac{1}{(4\pi)^2} \left[9(\gamma - 2 \ln 2) + \frac{19}{4} \right], \quad (17)$$

$$c_2(t) = \frac{1}{(4\pi)^2} \frac{33}{16}, \quad (18)$$

$$c_3(t) = \frac{1}{4} \left\{ 1 + \frac{\bar{g}(1/\sqrt{8t})^2}{(4\pi)^2} \left[2 + \frac{4}{3} \ln(432) \right] \right\}, \quad (19)$$

$$c_4(t) = \frac{1}{(4\pi)^2} \bar{g}(1/\sqrt{8t})^2, \quad (20)$$

$$c_5^f(t) = -\bar{m}_f(1/\sqrt{8t}) \left\{ 1 + \frac{\bar{g}(1/\sqrt{8t})^2}{(4\pi)^2} \left[4(\gamma - 2 \ln 2) + \frac{14}{3} + \frac{4}{3} \ln(432) \right] \right\}, \quad (21)$$

where γ denotes the Euler constant and $\bar{g}(\mu)$ and $\bar{m}_f(\mu)$ are the running gauge coupling and the running quark mass of the flavor f in the $\overline{\text{MS}}$ scheme at the scale μ , respectively.

In principle, one may use any lattice transcription for the composite operators in Eqs. (9)-(13) as well as for the flow equations (1), (4), and (5); in this sense, the above formula for the energy-momentum tensor is “universal”. This universality follows from the fact that any composite operator of the flowed fields becomes a renormalized operator [3, 4] under the multiplicative renormalization of the flowed quark fields (see also Ref. [28]). The normalization factor (15) takes care of this multiplicative renormalization of the flowed quark fields [9]. Such a renormalized composite operator must be independent of the regularization, i.e., the way of lattice discretization, for example, after taking the continuum limit.

C. Scalar density and the chiral condensate

In Ref. [10], the small flow time behavior of a composite operator of flowed quark fields is related to the quark scalar density. For the renormalized scalar density of the form (suppressing the flavor indices)

$$\{\bar{\psi}\{\{t^A, M\}, t^B\}\psi\}(x), \quad (22)$$

where t^A and t^B denote the (antihermitian) generators of the flavor group $SU(3)$ and M is the renormalized quark mass matrix of the form

$$M = \begin{pmatrix} m_{ud} & 0 & 0 \\ 0 & m_{ud} & 0 \\ 0 & 0 & m_s \end{pmatrix}, \quad (23)$$

one has

$$\begin{aligned}
& \{\bar{\psi}\{\{t^A, M\}, t^B\}\psi\}(x) \\
&= \lim_{t \rightarrow 0} \left\{ 1 + \frac{\bar{g}(1/\sqrt{8t})^2}{(4\pi)^2} \left[4(\gamma - 2 \ln 2) + 8 + \frac{4}{3} \ln(432) \right] \right\} \\
& \quad \times \left[\sum_{f, f'=u,d,s} \sqrt{\varphi_f(t)} \sqrt{\varphi_{f'}(t)} \bar{\chi}_f(t, x) \{\{t^A, \bar{M}(1/\sqrt{8t})\}, t^B\}_{ff'} \chi_{f'}(t, x) - \text{VEV} \right]. \quad (24)
\end{aligned}$$

In the last line, the vacuum expectation value (VEV) of the first term on the same line is subtracted. In the right-hand side, the running coupling $\bar{g}(\mu)$ and the running masses in the matrix \bar{M} ,

$$\bar{M}(\mu) = \begin{pmatrix} \bar{m}_{ud}(\mu) & 0 & 0 \\ 0 & \bar{m}_{ud}(\mu) & 0 \\ 0 & 0 & \bar{m}_s(\mu) \end{pmatrix}, \quad (25)$$

are renormalized in the $\overline{\text{MS}}$ scheme at the scale μ .

The relation (24) is obtained in the following way [10]: We define the scalar density (22) as the chiral rotation of the pseudoscalar density $\{\bar{\psi} \gamma_5 \{t^A, M\} \psi\}(x)$, where the chiral rotation is defined by

$$\psi(x) \rightarrow e^{\alpha \gamma_5 t^B} \psi(x), \quad \bar{\psi}(x) \rightarrow \bar{\psi}(x) e^{\alpha \gamma_5 t^B}, \quad (26)$$

and, correspondingly, for the flowed quark fields,

$$\chi(x) \rightarrow e^{\alpha \gamma_5 t^B} \chi(x), \quad \bar{\chi}(x) \rightarrow \bar{\chi}(x) e^{\alpha \gamma_5 t^B}. \quad (27)$$

The normalization of the pseudoscalar density is uniquely fixed by the PCAC relation. The small flow time representation of the pseudoscalar density was obtained in Ref. [29]. Because the composite operators of the flowed quark fields transform under the chiral transformation as if they are simple products of elementary quark fields (i.e., no nontrivial renormalization is required under the transformation), one obtains the relation (24) by the chiral transformation (27) of the pseudoscalar density.

This argument based on the chiral transformation does not necessarily require the subtraction of the VEV in Eq. (24). We have to note, however, that the flavor singlet part of the scalar density possesses the quantum number identical to the vacuum and, when quarks are massive, its expectation value can have terms proportional to M^2/t depending on the prescription, though the more conventional divergence M^2/a^2 is prohibited by the finiteness

of flowed operators.⁵ In fact, the small flow time behavior of the operator in the right-hand side of Eq. (24) is estimated as

$$\begin{aligned}
& \sum_{f,f'=u,d,s} \sqrt{\varphi_f(t)} \sqrt{\varphi_{f'}(t)} \bar{\chi}_f(t,x) \{ \{t^A, M\}, t^B \}_{ff'} \chi_{f'}(t,x) \\
& \stackrel{t \rightarrow 0}{\sim} \left[-\frac{12}{(4\pi)^2} \sum_{f=u,d,s} \left(\{ \{t^A, M\}, t^B \} M \left\{ \frac{1}{2t} + M^2 [\gamma + \ln(2M^2t)] + O(t) \right\} \right)_{ff} + O(g^2) \right] \mathbb{1} \\
& + [1 + O(g^2)] \bar{\psi}(x) \{ \{t^A, M\}, t^B \} \psi(x) + O(t). \tag{28}
\end{aligned}$$

Therefore, when quarks are massive, the first term with the identity operator $\mathbb{1}$ diverges as $t \rightarrow 0$. To remove such term, we subtract the VEV in Eq. (24). We may alternatively calculate the scalar density in the chiral limit, by first taking the chiral limit $M \rightarrow 0$ and then taking the small flow time limit $t \rightarrow 0$. We leave this possibility for future study.

Now, by setting

$$t^A = t^B = \frac{i}{2} \begin{pmatrix} 0 & 1 & 0 \\ 1 & 0 & 0 \\ 0 & 0 & 0 \end{pmatrix} \tag{29}$$

in Eq. (24) and dividing the both sides by m_u or m_d , we get

$$\begin{aligned}
& \{ \bar{\psi}_u \psi_u \}(x) + \{ \bar{\psi}_d \psi_d \}(x) \\
& = \lim_{t \rightarrow 0} \left\{ 1 + \frac{\bar{g}(1/\sqrt{8t})^2}{(4\pi)^2} \left[4(\gamma - 2 \ln 2) + 8 + \frac{4}{3} \ln(432) \right] \right\} \\
& \quad \times \frac{\bar{m}_{ud}(1/\sqrt{8t})}{m_{ud}} [\varphi_u(t) \bar{\chi}_u(t,x) \chi_u(t,x) + \varphi_d(t) \bar{\chi}_d(t,x) \chi_d(t,x) - \text{VEV}], \tag{30}
\end{aligned}$$

while by setting

$$t^A = t^B = \frac{i}{2} \frac{1}{\sqrt{3}} \begin{pmatrix} 1 & 0 & 0 \\ 0 & 1 & 0 \\ 0 & 0 & -2 \end{pmatrix} \tag{31}$$

and using Eq. (30), we get

$$\begin{aligned}
\{ \bar{\psi}_s \psi_s \}(x) & = \lim_{t \rightarrow 0} \left\{ 1 + \frac{\bar{g}(1/\sqrt{8t})^2}{(4\pi)^2} \left[4(\gamma - 2 \ln 2) + 8 + \frac{4}{3} \ln(432) \right] \right\} \\
& \quad \times \frac{\bar{m}_s(1/\sqrt{8t})}{m_s} [\varphi_s(t) \bar{\chi}_s(t,x) \chi_s(t,x) - \text{VEV}]. \tag{32}
\end{aligned}$$

⁵ We would like to thank Tetsuya Onogi and Hidenori Fukaya for a discussion on this point.

For clarity, let us denote the chiral condensate at $t \neq 0$ without the VEV subtraction as $\{\bar{\psi}_f \psi_f\}^{(0)}(t, x)$,

$$\begin{aligned} \{\bar{\psi}_f \psi_f\}^{(0)}(t, x) &= \left\{ 1 + \frac{\bar{g}(1/\sqrt{8t})^2}{(4\pi)^2} \left[4(\gamma - 2 \ln 2) + 8 + \frac{4}{3} \ln(432) \right] \right\} \\ &\quad \times \frac{\bar{m}_f(1/\sqrt{8t})}{m_f} [\varphi_f(t) \bar{\chi}_f(t, x) \chi_f(t, x)]. \end{aligned} \quad (33)$$

D. Finite flow time effects and lattice artifacts

To avoid boundary effects due to oversmearing, the smeared range of the gradient flow $\sqrt{8t}$ should not exceed $\min(N_t/2, N_s/2) \times a$. Thus, the measurements should be performed within flow times

$$\frac{t}{a^2} \leq t_{1/2} \equiv \frac{1}{8} \left[\min \left(\frac{N_t}{2}, \frac{N_s}{2} \right) \right]^2. \quad (34)$$

We then take the $t \rightarrow 0$ limit as required in Eq. (8). A typical form of small flow time effects in the energy-momentum tensor would be

$$T_{\mu\nu}(t, x) = T_{\mu\nu}(x) + t S_{\mu\nu}(x) + O(t^2), \quad (35)$$

where $T_{\mu\nu}(t, x)$ corresponds to that in Eq. (8) before taking the $t \rightarrow 0$ limit. $S_{\mu\nu}(x)$ is a sum of dimension-six operators with the same quantum number and $O(t^2)$ is contribution from higher dimensional operators. $T_{\mu\nu}(x)$ is our target conserved energy-momentum tensor.

On finite lattices, however, we also have lattice artifacts due to finite lattice spacing a . Since we adopt the nonperturbatively $O(a)$ -improved Wilson fermion, the lattice artifact would start with $O(a^2)$. Then, small lattice spacing corrections to $T_{\mu\nu}(t, x)$ at $t > 0$ would be

$$\begin{aligned} T_{\mu\nu}(t, x, a) &= T_{\mu\nu}(t, x) + A_{\mu\nu}(x) \frac{a^2}{t} + \sum_f B_{f\mu\nu}(x) (am_f)^2 + C_{\mu\nu}(x) (aT)^2 \\ &\quad + D_{\mu\nu}(x) (a\Lambda_{\text{QCD}})^2 + a^2 S'_{\mu\nu}(x) + O(a^4), \end{aligned} \quad (36)$$

where $T_{\mu\nu}(t, x, a)$ is the flowed tensor operator on the lattice. $A_{\mu\nu}$, $B_{f\mu\nu}$, $C_{\mu\nu}$, and $D_{\mu\nu}$ are contributions from dimension-four operators and $S'_{\mu\nu}$ is that from dimension-six operators. We note that the a^2/t term can appear to the lowest order in a^2 through mixing with dimension-four operators. In the higher orders in a^2 , more singular terms like $1/t^2$ can enter.

When we take the continuum limit before taking the $t \rightarrow 0$ limit, the $O(a^2)$ terms in Eq. (36), including all the singular terms at $t = 0$, are removed, and we can carry out the $t \rightarrow 0$ extrapolation safely. In numerical simulations, however, it is sometimes favorable to take the continuum extrapolation at a later stage of analyses. This exchange of the order of limiting procedures is allowed if we can remove the singular terms at $t = 0$. We come back to this issue in the actual $t \rightarrow 0$ extrapolations in Sec. IV.

Similar to the case of the energy-momentum tensor, the chiral condensate on finite lattices is expected to be

$$\begin{aligned} \{\bar{\psi}_f \psi_f\}^{(0)}(t, x, a) &= \{\bar{\psi}_f \psi_f\}^{(0)}(t, x) + A(x) \frac{a^2}{t} + \sum_f B_f(x) (am_f)^2 \\ &+ C(x) (aT)^2 + D(x) (a\Lambda_{\text{QCD}})^2 + a^2 S(x) + O(a^4) \end{aligned} \quad (37)$$

to the lowest order of a^2 , where $\{\bar{\psi}_f \psi_f\}^{(0)}(t, x, a)$ is the flowed operator at finite lattice spacing before the VEV subtraction. A , B_f , C , and D are contributions from dimension-three operators and S is that from dimension-five operators. After taking the continuum limit, the scalar density should be given by

$$\{\bar{\psi}_f \psi_f\}^{(0)}(t, x) = \{\bar{\psi}_f \psi_f\}_{\overline{\text{MS}}}(x) + \frac{m_f}{t} N(x) + t S'(x) + O(t^2), \quad (38)$$

where $\{\bar{\psi}_f \psi_f\}_{\overline{\text{MS}}}(x)$ is the renormalized chiral condensate in $\overline{\text{MS}}$ scheme. N is a contribution of dimensionless operators and S' is that from dimension-five operators. Thus, $\{\bar{\psi}_f \psi_f\}^{(0)}(t, x, a)$ at finite lattice spacing and finite quark mass has both m_f/t and a^2/t singularities around the origin.

When we take the chiral and continuum limits before taking the $t \rightarrow 0$ limit, these singular terms of the chiral condensate at $t = 0$ are removed, and we can do the $t \rightarrow 0$ extrapolation safely. Conversely, when we can remove the singular terms at $t = 0$, we can exchange the order of the three limiting procedures. The m_f/t singularity can be removed by the VEV subtraction discussed in Sec. II C. Because the lattice spacing is the same in the VEV, we expect that the a^2/t singularity is also in part removed by the VEV subtraction. We study this issue with the actual data in Sec. V.

III. SIMULATION PARAMETERS AND NUMERICAL PROCEDURES

Measurements of the energy-momentum tensor are performed on $N_f = 2 + 1$ gauge configurations generated for Ref. [30]. In these calculations, we need to subtract the zero-temperature values of the operators. The zero temperature gauge configurations are also prepared which were generated for Ref. [31]. These configurations are open to the public on ILDG/JLDG [32].

The nonperturbatively $O(a)$ -improved Wilson quark action [33] and the renormalization-group improved Iwasaki gauge action [34, 35] are adopted. The bare coupling constant is set to $\beta = 2.05$, which corresponds to $a = 0.0701(29)$ fm ($1/a \simeq 2.79$ GeV) with an input of $r_0 = 0.5$ fm [36]. The nonperturbative clover coefficient is $c_{\text{SW}} = 1.628$ at $\beta = 2.05$, which is determined by the Schrödinger functional method [37]. The hopping parameters are set to $\kappa_u = \kappa_d \equiv \kappa_{ud} = 0.1356$ and $\kappa_s = 0.1351$, which correspond to heavy u and d quarks, $m_\pi/m_\rho \simeq 0.63$, and almost physical s quark, $m_{\eta_{ss}}/m_\phi \simeq 0.74$, where η_{ss} is the strange pseudoscalar meson whose mass is phenomenologically estimated as $m_{\eta_{ss}} \approx \sqrt{2m_K^2 - m_\pi^2}$. The bare PCAC quark masses are

$$a m_{ud} = 0.02105(17), \quad a m_s = 0.03524(26), \quad (39)$$

where $m_{ud} = m_u = m_d$ is the degenerate mass of u and d quarks [31].

In this study, we adopt the fixed-scale approach [13, 23] in which the temperature $T = 1/(aN_t)$ is varied by changing the temporal lattice size N_t with a fixed lattice spacing a . This enables us to use one common zero-temperature simulation to subtract zero-temperature contributions at all temperatures. The equation of state using the T -integration method [13] was obtained previously using the same set of configurations [30].

The values of temperature at each N_t are given in Table I. In the table, T/T_{pc} assuming the pseudocritical temperature to be $T_{\text{pc}} = 190$ MeV [30] is also listed. The spatial box size is 32^3 for $T > 0$ and 28^3 for $T = 0$. The values of $t_{1/2}$ defined by Eq. (34) are also given in the Table.

The gauge observables (9) and (10) are measured every five trajectories at $T > 0$ and every ten trajectories at $T = 0$. The fermionic observables (11), (12), and (13) are measured every 50 trajectories at $T > 0$ and every 100 trajectories at $T = 0$. Number of configurations used for gauge and fermion measurements are summarized in Table I.

TABLE I. Parameters for the numerical simulation: Temperature in MeV, T/T_{pc} assuming $T_{\text{pc}} = 190$ MeV, the temporal lattice size N_t , $t_{1/2}$ defined by Eq. (34), and the number of configurations used in gauge and fermion measurements. The bare gauge coupling parameter and the hopping parameters are set to $\beta = 2.05$, $\kappa_{ud} = 0.1356$, and $\kappa_s = 0.1351$. Spatial box size is 32^3 for $T > 0$ and 28^3 for $T = 0$.

| $T[\text{MeV}]$ | T/T_{pc} | N_t | $t_{1/2}$ | Gauge configurations | Fermion configurations |
|-----------------|-------------------|-------|-----------|----------------------|------------------------|
| 0 | 0 | 56 | 24.5 | 650 | 65 |
| 174 | 0.92 | 16 | 8 | 1440 | 144 |
| 199 | 1.05 | 14 | 6.125 | 1270 | 127 |
| 232 | 1.22 | 12 | 4.5 | 1290 | 129 |
| 279 | 1.47 | 10 | 3.125 | 780 | 78 |
| 348 | 1.83 | 8 | 2 | 510 | 51 |
| 464 | 2.44 | 6 | 1.125 | 500 | 50 |
| 697 | 3.67 | 4 | 0.5 | 700 | 70 |

Our numerical procedures to compute the fermionic observables (11), (12), and (13) at $t > 0$ are given in Appendix A. To evaluate fermionic observables, we use the noisy estimator method. The number of noise vectors is 20 for each color. To reduce correlation among data points at different values of t , we generate independent noise vectors at each t . The statistical errors are estimated by the standard jackknife analysis. After a study of the bin size dependence, we choose the bin size of 100 trajectories for the energy-momentum tensor and 300 trajectories for the chiral condensate and susceptibility.

To compute observables at $t > 0$, we need flowed gauge and quark fields. Our numerical algorithm for gradient flow of gauge and quark fields is summarized in Appendix B. We adopt the third order Runge-Kutta method [2, 4] with the step size of $\epsilon = 0.02$ to solve the differential equation for both the gauge and quark fields.

For the flowed operators $\tilde{\mathcal{O}}_{i\mu\nu}(t, x)$ in Eqs. (9)-(13), we adopt the lattice symmetric covariant differential. For the quadratic terms of the field strength tensor $G_{\mu\nu}(x)$ in Eqs. (9) and (10), there are several alternative choices of lattice operators. In this study, we combine clover operator with four plaquette Wilson loops and that with eight 1×2 rectangle Wilson loops such that the tree-level improved field strength squared is obtained [38].

IV. RESULTS FOR THE ENERGY-MOMENTUM TENSOR

The pressure and the energy density are given by an averaged spatial component of the energy-momentum tensor and the temporal component of the energy-momentum tensor,

$$p/T^4 = \sum_i \langle T_{ii} \rangle / (3T^4), \quad \epsilon/T^4 = -\langle T_{00} \rangle / T^4. \quad (40)$$

In Figs. 1 and 2, we show the results of the entropy density

$$\frac{\epsilon + p}{T^4} = -\frac{4}{3T^4} \left\langle T_{00} - \frac{1}{4} T_{\mu\mu} \right\rangle \quad (41)$$

and the trace anomaly

$$\frac{\epsilon - 3p}{T^4} = -\frac{1}{T^4} \langle T_{\mu\mu} \rangle \quad (42)$$

as functions of t/a^2 . Seven subplots in each figure are for the results at $T \simeq 174, 199, 232, 279, 348, 464,$ and 697 MeV ($N_t = 16, 14, 12, 10, 8, 6$ and 4 , respectively) from the top left to the bottom. The errors shown are statistical only.

A. Extrapolation to $t \rightarrow 0$

We extract physical results for the energy-momentum tensor by extrapolating the data to $t \rightarrow 0$. As discussed in Sec. IID, on finite lattices, we have to take care of unphysical singularities like a^2/t around the origin. On the other hand, our data shown in the figures indicates that, except for the case of the highest temperature $T \simeq 697$ MeV ($N_t = 4$), we do have ranges of t/a^2 in which the data show well linear behavior. This suggests that the singular terms like a^2/t are numerically negligible when t/a^2 is not so small.

We first identify linear windows from the data shown in Figs. 1 and 2 as ranges in t/a^2 in which the data are well linear under the condition that $t/a^2 < t_{1/2}$. The windows are selected such that the linear fit discussed in the following leads to $\chi^2/N_{\text{dof}} \leq O(1)$. We also require that the window is common to all components of the energy-momentum tensor on each lattice. The results for the linear window are shown by a pair of dashed vertical lines in Figs. 1 and 2, except for the case of $T \simeq 697$ MeV ($N_t = 4$) for which no clear linear window is visible below $t_{1/2} = 0.5$. We note that the case of $T \simeq 464$ MeV ($N_t = 6$) may be marginal to clearly identify a wide linear window because $t_{1/2} = 1.125$ for this lattice is also small.

At $T \lesssim 464$ MeV, we perform a linear extrapolation

$$\langle T_{\mu\nu}(t, a) \rangle = \langle T_{\mu\nu} \rangle + t S_{\mu\nu} + O(a^2, t^2) \quad (43)$$

adopting the linear windows of Figs. 1 and 2, to obtain the physical results $\langle T_{\mu\nu} \rangle$ for the energy-momentum tensor. Our linear fits and the results of extrapolation are shown by black solid lines and big open circles at $t = 0$ in Figs. 1 and 2.⁶ We note that the data at $T \lesssim 232$ MeV are well flat within the window. In fact, a constant fit leads to results consistent with the linear fit within statistical errors.

To confirm the validity of the linear window and to estimate a systematic error due to the fit Ansatz, we also make additional fits adopting two different fit Ansätze using the data within the same window. One is a nonlinear fit inspired from Eq. (36),

$$\langle T_{\mu\nu}(t, a) \rangle = \langle T_{\mu\nu} \rangle + A_{\mu\nu} \frac{a^2}{t} + t S_{\mu\nu} + t^2 R_{\mu\nu}. \quad (44)$$

Another is a linear+log fit including an additional $1/\log^2(\sqrt{8t}/a)$ term,

$$\langle T_{\mu\nu}(t, a) \rangle = \langle T_{\mu\nu} \rangle + t S_{\mu\nu} + \frac{Q_{\mu\nu}}{\log^2(\sqrt{8t}/a)}. \quad (45)$$

The latter is inspired from possible higher order corrections to the matching coefficients $c_i(t)$ in Eqs. (17)–(21), which are computed in one-loop perturbation theory [9] in our study. As discussed in Ref. [39] [Eq. (7.14)], for a small but finite flow time t , those perturbative one-loop coefficients may contain error of the order $\bar{g}(1/\sqrt{8t})^4/(4\pi)^4 \sim 1/\log^2(t)$ associated with neglected higher-order loop corrections. Though higher-order perturbative corrections should be subdominant at small t because of the asymptotic freedom, the formula (35) thus may in principle be modified by $O(1/\log^2(t))$ terms. A fit including all the correction terms in (44) and (45) turned out to be unstable due to too many fitting parameters.

The results of the nonlinear and linear+log fits for the entropy density and the trace anomaly at $T \lesssim 464$ MeV ($N_t \geq 6$) are shown by blue and green dashed curves in Figs. 1 and 2, respectively. In these figures, physical results $\langle T_{\mu\nu} \rangle$ extracted from these fits are shown by blue upward triangles and green diamonds at $t \sim 0$. We find that all the three

⁶ As in the previous study in quenched QCD [19], we disregard correlation among different flow times in this study. Our introduction of independent noise vectors at each t should reduce the correlation in fermionic contributions. The jagged behavior visible, e.g., in Fig. 2 may be suggesting that the correlation is small in several observables. However, we find that our statistics is not high enough to discuss the correlation conclusively. We leave the study of the correlation for the next step.

fits are almost indistinguishable in the windows and describe the data within the windows well. We also note that the nonlinear fit frequently fails to reproduce the singular behavior at small t/a^2 out of the linear window. On the other hand, the linear+log fit stays close to the linear fit down to small t in most cases, but can slightly deviate when the data are noisy, as seen in Fig. 2.

At $T \lesssim 464$ MeV ($N_t \geq 6$), we adopt the results of the linear fit for our central values and take the difference between the linear fit and the nonlinear or linear+log fits as an estimate of the systematic error due to the choice of the fit Ansatz. We find that the differences are at most a few times of the statistical error at $T \lesssim 232$ MeV ($N_t \geq 12$), while a larger difference can appear at higher temperatures.⁷

Finally, we estimate the systematic error from the one-loop perturbative coefficients themselves. For the perturbative coefficients, Eqs. (17)–(21), we need to know the running gauge coupling $\bar{g}(1/\sqrt{8t})$ and the running quark masses $\bar{m}_f(1/\sqrt{8t})$. Definitions of these running coupling and running masses are given in Appendix C. Inputs for $\bar{g}(\mu)$ and $\bar{m}_f(\mu)$ are the QCD scale Λ_{QCD} and the bare quark masses. For the QCD scale, we refer the value quoted in the Particle Data Group [40]

$$\Lambda_{\overline{\text{MS}}}^{(3)} = 332(19) \text{ MeV}. \quad (46)$$

Since $1/\sqrt{8t}$ plays a role of the renormalization scale, the QCD scale appears with the form $a\sqrt{8(t/a^2)}\Lambda_{\text{QCD}}$ in the perturbative coefficients, where t/a^2 is a dimensionless flow time used on the lattice. In this combination of the QCD scale, we should take into account the statistical error in the lattice spacing. As the bare quark masses, we use the PCAC masses of Eq. (39) obtained on the same zero-temperature configuration as ours [31]. In the running quark masses, the bare quark masses appear in the combination of renormalization group invariant masses, for which we should take into account the error in the renormalization factor too. The values as well as the errors for $\bar{g}(\mu)$ and $\bar{m}_f(\mu)$ are estimated in Appendix C.

Our results of the equation of state in the $t \rightarrow 0$ limit are summarized in Table II and III. In this table, we give the values of statistical error as well as the systematic errors due to the perturbative coefficients and the fit Ansatz, separately.

At $T \simeq 697$ MeV ($N_t = 4$), because a clear linear window is not available, we attempt a fit of the form (44) adopting a fit range $t/a^2 = [0.1, 0.5 = t_{1/2}]$ shown by dashed vertical lines

⁷ We should, however, notice that the lattice artifacts $B_{f\mu\nu}(am_f)^2 + C_{\mu\nu}(aT)^2 + D_{\mu\nu}(a\Lambda_{\text{QCD}})^2 + a^2 S'_{\mu\nu}(x)$ of Eq. (36) still remain and can be settled only after taking the continuum limit.

in the bottom plots of Figs. 1 and 2, but with dropping the t^2 term to keep a nonvanishing DOF. The results of $\langle T_{\mu\nu} \rangle$ are shown by blue upward triangles at $t \sim 0$ in these plots. As seen from the resulting fits shown by dashed curves, although the nonlinear fit Ansatz describes the data at small t well, the lattice artifact term is completely dominating over the linear term which contain physical information. We thus consider that the results at $T \simeq 697$ MeV ($N_t = 4$) are not reliable and disregard them in the followings.

TABLE II. Equation of state (pressure and energy density) evaluated with the gradient flow method in the $t \rightarrow 0$ limit. The first parenthesis is for the statistical error estimated by a jackknife method. The second and the third are for systematic errors due to $\Lambda_{\overline{\text{MS}}}^{(3)}$ and the bare quark masses in the perturbative coefficients. The last parenthesis is for the systematic error due to the fit Ansatz estimated using Eqs. (44) and (45).

| $T[\text{MeV}]$ | p/T^4 | ϵ/T^4 |
|-----------------|--|---|
| 174 | 0.13(60) $^{(+4)}_{(-1)}(1)^{(+0)}_{(-15)}$ | 2.75(68) $^{(+8)}_{(-14)}(1)^{(+30)}_{(-89)}$ |
| 199 | -0.42(41) $^{(+5)}_{(-0)}(4)^{(+66)}_{(-19)}$ | 8.54(57) $^{(+15)}_{(-24)}(4)^{(+21)}_{(-70)}$ |
| 232 | 1.12(30) $^{(+5)}_{(-4)}(5)^{(+0)}_{(-23)}$ | 13.07(38) $^{(+11)}_{(-14)}(5)^{(+54)}_{(-36)}$ |
| 279 | 2.46(19) $^{(+6)}_{(-5)}(3)^{(+0)}_{(-52)}$ | 14.74(25) $^{(+14)}_{(-17)}(3)^{(+0)}_{(-1.68)}$ |
| 348 | 5.00(10) $^{(+4)}_{(-3)}(2)^{(+31)}_{(-2.63)}$ | 16.15(13) $^{(+19)}_{(-23)}(2)^{(+1.36)}_{(-31)}$ |
| 464 | 7.596(65) $^{(+11)}_{(-4)}(9)^{(+1)}_{(-33)}$ | 19.92(8)(14)(1) $^{(+42)}_{(-77)}$ |

TABLE III. The same as Table II but for the entropy density and trace anomaly evaluated with the gradient flow method in the $t \rightarrow 0$ limit.

| $T[\text{MeV}]$ | $(\epsilon + p)/T^4$ | $(\epsilon - 3p)/T^4$ |
|-----------------|--|---|
| 174 | 2.90(43) $^{(+7)}_{(-11)}(0)^{(+76)}_{(-0)}$ | 2.4(2.4) $^{(+1)}_{(-2)}(0)^{(+7)}_{(-0)}$ |
| 199 | 8.09(41) $^{(+15)}_{(-20)}(0)^{(+5)}_{(-17)}$ | 9.8(1.7) $^{(+1)}_{(-4)}(1)^{(+8)}_{(-2.8)}$ |
| 232 | 14.25(28) $^{(+16)}_{(-17)}(0)^{(+91)}_{(-67)}$ | 9.7(1.2)(0)(2) $^{(+3)}_{(-0)}$ |
| 279 | 17.29(23) $^{(+19)}_{(-21)}(0)^{(+0)}_{(-1.80)}$ | 7.38(73) $^{(+0)}_{(-3)}(14)^{(+1.31)}_{(-0)}$ |
| 348 | 21.25(12) $^{(+21)}_{(-24)}(0)^{(+0)}_{(-63)}$ | 1.00(37) $^{(+8)}_{(-14)}(7)^{(+4.33)}_{(-1.08)}$ |
| 464 | 27.53(8) $^{(+15)}_{(-14)}(0)^{(+0)}_{(-85)}$ | -2.87(23) $^{(+10)}_{(-13)}(4)^{(+0)}_{(-1.16)}$ |

B. Additional tests

To confirm the validity of the results, we made a couple of additional tests on our numerical data. The results of the tests are summarized in Appendix D.

Off diagonal components of the energy-momentum tensor correspond to the momentum and stress density, which should vanish on our lattices without external sources. As discussed in Appendix D 1, we confirm that they are consistent with zero within 2σ in the window adopted in the fits in Sec. IV A.

We also study the gauge and quark contributions in Eq. (8) separately, and find that both contributions are equally important in the equation of state, while the singular term a^2/t comes dominantly from the quark contributions. See Appendix D 2 for details.

Finally, we examine if the results depend on the choice of lattice operators for the field strength squared in Eqs. (9) and (10) in Appendix D 3. We confirm that the dependence is small.

C. Equation of state

Our results for the equation of state with the gradient flow method are plotted in Figs. 3, 4, 5, and 6 as functions of temperature. For the pressure and the energy density, we have repeated the same set of analyses from the results of the energy-momentum tensor at $t > 0$. Errors of our data (red open circles) include the statistical error and the systematic errors from the perturbative coefficients and fit Ansatz.

Also shown in these figures by open triangles are the results obtained previously by the T -integration method using the same set of configurations [30]. We find that our result of the gradient flow method is well consistent with the result of the conventional method at $T \lesssim 279$ MeV. On the other hand, the two results show a deviation at $T \gtrsim 348$ MeV. This may be due to a lattice artifact of $O((aT)^2) = O(1/N_t^2)$ from the discretization of thermal modes. Our data suggest that such an artifact is not negligible for $N_t \lesssim 8$.

It should be kept in mind that a definite comparison is possible only after taking the continuum limit. Nevertheless, besides the results at $N_t \lesssim 8$ which suffer from the small- N_t artifact, we obtain good agreement with a conventional method at $N_t \gtrsim 10$ on our finite lattices. This may be suggesting that our $a \simeq 0.07$ fm with improved gauge and quark

actions is already quite close to the continuum limit.

Here, we emphasize that the values of the beta functions — $a(d\beta/da)$, $a(d\kappa_{ud}/da)$, and $a(d\kappa_s/da)$ for the present case — are not required with the gradient flow method. This will help much to evaluate the equation of state with dynamical quarks in future.

V. RESULTS FOR THE CHIRAL CONDENSATE AND DISCONNECTED SUSCEPTIBILITY

A. Chiral condensate

In Fig. 7, we show the VEV subtracted chiral condensate at $T > 0$ as a function of the flow time. We note that the singularity at small t is quite mild in the subtracted chiral condensate at least at low temperatures. This suggests that the VEV subtraction not only removes the m_f/t singularity but also reduces the a^2/t singularity.

We adopt the same strategy as that for the energy-momentum tensor to extract renormalized chiral condensate with the VEV subtraction. In Fig. 7, results of the linear fits using windows shown by a pair of vertical dashed lines, are given by red and black solid lines for $T \lesssim 464$ MeV. Here, the windows are chosen so that the linear fit gives $\chi^2/N_{\text{dof}} \leq O(1)$. The filled red circles and black triangles at $t = 0$ are the results of their $t \rightarrow 0$ extrapolations. We also perform nonlinear fits similar to Eq. (44) and liner+log fits similar to Eq. (45), adopting the same window. The results of nonlinear fits are shown by orange and blue dashed curves, and corresponding renormalized chiral condensates are shown by orange and blue open symbols at $t \sim 0$. The results of linear+log fits are shown by magenta and green dashed curves associated with open symbols at $t \sim 0$. At $T \simeq 464$ MeV, the nonlinear and linear+log fits are not applicable because we do not have enough number of data points in the window ($N_{\text{dof}} \leq 1$).

From Fig. 7, we find that the results of the nonlinear and the linear+log fits at $T \lesssim 348$ MeV are consistent with those of the linear fits within 2σ of the statistical error. We adopt the results of the linear fit for our central values and take the deviation due to the nonlinear or linear+log fits as an estimate of the systematic error due to the fit Ansatz. Final results for the renormalized chiral condensate with the VEV subtraction, $\langle \{\bar{\psi}_f \psi_f\}(x) \rangle_{\overline{\text{MS}}}(\mu = 2\text{GeV})$ with $f = u$ (or d) and s , evaluated in the $t \rightarrow 0$ limit, are summarized in Tables IV and

V. In Fig. 8, we show the renormalized chiral condensates with the VEV subtraction in physical units as a function of the temperature. Following a convention, the sign is flipped in the figure. We find that the condensates start to decrease just below $T \sim 199$ MeV. This is consistent with a previous estimation of the pseudocritical temperature $T_{pc} \sim 190$ MeV [30]. We also find that the valence quark mass dependence is small in Fig. 8. This suggests that the difference between these two condensates are mostly subtracted out by that at zero temperature, i.e. the mass dependent part of the chiral condensate is almost temperature independent.

TABLE IV. Renormalized chiral condensate with the VEV subtraction and disconnected chiral susceptibility for u (or, equivalently, d) quark, evaluated in the $t \rightarrow 0$ limit. The values are in lattice unit. The susceptibility is given in a unit of 10^{-8} . The first parenthesis is for the statistical error. The second is for systematic error due to $a\Lambda_{\overline{\text{MS}}}^{(3)}$ in the perturbative coefficients. The last parenthesis is that due to the fit Ansatz estimated using nonlinear and linear+log fits. At $T \simeq 464$ MeV, the systematic error due to fit Ansatz was not estimated. See text.

| T [MeV] | $a^3 \langle \{\bar{\psi}_u \psi_u\}(x) \rangle_{\overline{\text{MS}}}$ | $a^6 \chi_{uu}^{\text{disc.}} \times 10^8$ |
|-----------|---|---|
| 0 | 0 | 0.46(15) $^{(+4)}_{(-10)}$ $^{(+2)}_{(-0)}$ |
| 174 | 0.000094(28) $^{(+28)}_{(-5)}$ $^{(+0)}_{(-12)}$ | 2.19(80) $^{(4)}_{(15)}$ $^{(+0)}_{(-23)}$ |
| 199 | 0.000500(53) $^{(+9)}_{(-19)}$ $^{(+0)}_{(-47)}$ | 5.0(1.7) $^{(+1)}_{(-4)}$ $^{(+0)}_{(-5)}$ |
| 232 | 0.000967(40) $^{(+26)}_{(-51)}$ $^{(+0)}_{(-34)}$ | 1.35(30) $^{(+7)}_{(-19)}$ $^{(+1)}_{(-0)}$ |
| 279 | 0.001413(42) $^{(+29)}_{(-58)}$ $^{(+0)}_{(-62)}$ | 1.04(32) $^{(+0)}_{(-3)}$ $^{(+2)}_{(-0)}$ |
| 348 | 0.001744(44) $^{(+46)}_{(-90)}$ $^{(+0)}_{(-55)}$ | 1.07(24) $^{(+4)}_{(-5)}$ $^{(+0)}_{(-10)}$ |
| 464 | 0.002800(44) $^{(+9)}_{(-31)}$ $^{(-)}$ | 1.27(13)(7) $^{(-)}$ |

At $T \simeq 697$ MeV ($N_t = 4$), because no clear linear window can be identified below $t_{1/2} = 0.5$, we attempt a nonlinear fit without the t^2 term adopting the same fit range $t = [0.1, 0.5]$ as in Sec. IV A. The results are shown in the last panel of Fig. 7. However, since the lattice artifact terms are dominating in the fit range, we disregard the data at $T \simeq 697$ MeV in the followings.

TABLE V. The same as Table IV but for s quark.

| T [MeV] | $a^3 \langle \{\bar{\psi}_s \psi_s\}(x) \rangle_{\overline{\text{MS}}}$ | $a^6 \chi_{\overline{\text{MS}}}^{\text{disc.}} \times 10^8$ |
|-----------|---|--|
| 0 | 0 | 0.320(88) $^{(+20)}_{(-51)}$ $^{(+17)}_{(-0)}$ |
| 174 | 0.000066(21) $^{(+2)}_{(-4)}$ $^{(+38)}_{(-9)}$ | 1.41(43) $^{(+0)}_{(-6)}$ $^{(+0)}_{(-16)}$ |
| 199 | 0.000396(41) $^{(+7)}_{(-15)}$ $^{(+0)}_{(-38)}$ | 3.3(1.0) $^{(+0)}_{(-2)}$ $^{(+0)}_{(-4)}$ |
| 232 | 0.000823(31) $^{(+23)}_{(-44)}$ $^{(+0)}_{(-28)}$ | 1.04(19) $^{(+5)}_{(-14)}$ $^{(+1)}_{(-0)}$ |
| 279 | 0.001325(35) $^{(+29)}_{(-57)}$ $^{(+0)}_{(-52)}$ | 0.90(25) $^{(+0)}_{(-4)}$ $^{(+4)}_{(-0)}$ |
| 348 | 0.001794(38) $^{(+52)}_{(-99)}$ $^{(+0)}_{(-60)}$ | 1.07(26) $^{(+4)}_{(-5)}$ $^{(+0)}_{(-11)}$ |
| 464 | 0.003170(38) $^{(+14)}_{(-41)}$ (-) | 1.30(15)(7)(-) |

B. Disconnected chiral susceptibility

As a by-product of the chiral condensate calculation, we study disconnected chiral susceptibility defined by

$$\chi_{ff}^{\text{disc.}} = \left\langle \left[\frac{1}{N_\Gamma} \sum_x \{\bar{\psi}_f \psi_f\}(x) \right]^2 \right\rangle_{\text{disconnected}} - \left[\left\langle \frac{1}{N_\Gamma} \sum_x \{\bar{\psi}_f \psi_f\}(x) \right\rangle \right]^2, \quad (47)$$

where the connected quark loop contribution is dropped from the scalar density two point function. Though this quantity is not the physical susceptibility, it is easy to be measured and may be used as a guide to detect the chiral restoration transition. Because the VEV subtraction has no effect on this quantity, we can compute it also at $T = 0$.

In Fig. 9, we plot the disconnected chiral susceptibility as a function of the flow time. We find good linear windows below $t_{1/2}$ at $T \lesssim 348$ MeV ($N_t \geq 8$) and a marginal window at $T \simeq 464$ MeV ($N_t = 6$), while at $T \simeq 697$ MeV ($N_t = 4$) no linear window can be identified below $t_{1/2} = 0.5$. We find that the linear and nonlinear fits give completely consistent results for $T \lesssim 348$ MeV, while the linear+log fit sometimes deviate but maximally by about 1σ of the statistical error. At $T \simeq 464$ MeV, the number of data points in the window is not enough to carry out the nonlinear as well as the linear+log fits. At $T \simeq 697$ MeV, though we test the nonlinear fit adopting the same fit range $t = [0.1, 0.5]$ as in Secs. IV A and V A, because the lattice artifact term is dominating in the fit as shown in the last plot of Fig. 9, we do not take the result as reliable and just disregard it.

Results of the renormalized disconnected chiral susceptibility are summarized in the last columns of Tables IV and V, and shown in Fig. 10 as a function of temperature. Errors

include the statistical error and the systematic errors from the perturbative coefficients and the fit Ansatz. In Fig. 10, we find a clear peak at $T \simeq 199$ MeV, which may be indicating the pseudocritical point around this temperature. This is consistent with a previous estimate of $T_{\text{pc}} \sim 190$ MeV for the chiral restoration crossover [30]. We also note that, although the errors are large, the height of the peak increases as we decrease the valence quark mass from that of s to u (or d). Since the sea quark masses are not varied, we do not attempt to extrapolate the results to the chiral limit, but the tendency is consistent with our expectation.

C. Chiral condensate without the VEV subtraction

Finally, we examine the effect of the VEV subtraction in the chiral condensate. In Fig. 11, we show the unsubtracted chiral condensate $\langle \{\bar{\psi}_f \psi_f\}^{(0)}(t, x, a) \rangle$ averaged over lattice points. Red open circles and black open triangles are for $f = u$ (or d) and s , respectively. As discussed in Secs. II C and II D, this quantity will have both m_f/t and a^2/t singularities towards $t \rightarrow 0$. We note that the singularity of the subtracted chiral condensate shown in Fig. 7 at small t is much milder than that of the unsubtracted chiral condensate shown in Fig. 11, suggesting that the VEV subtraction not only removes the m_f/t singularity but also reduces the a^2/t singularity, as expected.

Adopting the same strategy as those for the energy-momentum tensor and the subtracted chiral condensate, we perform linear and nonlinear fits to the unsubtracted chiral condensate, to extract the renormalized chiral condensate in the $t \rightarrow 0$ limit. The linear windows determined by a study of χ^2/N_{dof} of the linear fits are shown by the pair of vertical dashed lines in Fig. 11. We note that the values of χ^2/N_{dof} are in general worse than those for the subtracted chiral condensate, presumably due to the stronger singularities. Results of the linear fits for the renormalized chiral condensate are shown by filled red circles (u or d quark) and black triangles (s quark) at $t = 0$ in Fig. 11.⁸ Corresponding results of the nonlinear fits are shown by green and blue open symbols at $t \sim 0$ for $T \lesssim 348$ MeV. At $T \simeq 464$ MeV, the nonlinear fit is not applicable because we do not have enough number of data points in the window. At $T \simeq 697$ MeV ($N_t = 4$), though we attempt a nonlinear fit

⁸ χ^2/N_{dof} of the linear fits are less than 5, except for those for the strange quark condensate at $T = 0$ and condensates at $T = 464$ MeV, for which χ^2/N_{dof} exceed 10.

using the data in $t = [0.1, 0.5]$, because the lattice artifact term is dominating in the fit, the results are not reliable for physical discussions.

At $T \lesssim 348$ MeV, the discrepancy between the two fit Ansätze turned out to be 2%–5%. This suggests that the singular terms in the unsubtracted chiral condensate are well controlled within the linear windows. As in the previous sections, we take the results of the linear fits as the central values and take the difference between the linear and nonlinear fits as an estimate of the systematic error due to the fit Ansatz. The results for the renormalized chiral condensate without the VEV subtraction, $\langle \{\bar{\psi}\psi\}(x) \rangle_{\overline{\text{MS}}}^{(0)}$ ($\mu = 2$ GeV), are shown by red circles (u or d quark) and black upward triangles (s quark) in Fig. 12. At $T = 0$, we obtain

$$a^3 \langle \{\bar{\psi}_u \psi_u\}(x) \rangle_{\overline{\text{MS}}}^{(0)} \Big|_{T=0} = -0.006841(33)_{(-0)}^{(+82)}_{(-170)}^{(+84)}, \quad (48)$$

$$a^3 \langle \{\bar{\psi}_s \psi_s\}(x) \rangle_{\overline{\text{MS}}}^{(0)} \Big|_{T=0} = -0.008803(24)_{(-0)}^{(+94)}_{(-235)}^{(+159)}. \quad (49)$$

The first parenthesis is for the statistical error, the second is for the systematic error due to $a\Lambda_{\overline{\text{MS}}}^{(3)}$ in the perturbative coefficients, and the third is for the systematic error due to fit Ansatz estimated using nonlinear and linear+log fits.

To compare the results of the unsubtracted chiral condensate with those of the subtracted chiral condensate discussed in Sec. V A, we add back the VEV's given by Eqs. (48) and (49) to the results of the subtracted chiral condensate shown in Fig. 8. Results are shown by orange diamonds (u or d quark) and blue downward triangles (s quark) in Fig. 12. We find that the results are completely consistent with those of direct fits to the unsubtracted chiral condensate.

VI. CONCLUSIONS AND DISCUSSIONS

In this paper we apply the gradient flow method of Refs. [9, 16] to calculate the energy-momentum tensor in $(2 + 1)$ -flavor QCD. As the first test of energy-momentum tensor evaluation in full QCD with the gradient flow method, we choose a simulation point used in our previous study of the equation of state with degenerate heavy u and d quarks and almost physical s quark: $m_\pi/m_\rho \simeq 0.63$ and $m_{\eta_{ss}}/m_\phi \simeq 0.74$ at a single but fine lattice spacing $a \simeq 0.07$ fm.

The pressure, energy density, entropy density and trace anomaly are studied as a function

of temperature. We found that the results of the gradient flow method are consistent with those of the T -integration method at low temperatures $T \lesssim 280$ MeV ($N_t \gtrsim 10$). However, deviation is found at high temperatures $T \gtrsim 350$ MeV ($N_t \lesssim 8$). This may be due to a lattice artifact of $O((aT)^2) = O(1/N_t^2)$ from the discretization of thermal modes, which becomes severe at high temperature in the fixed-scale approach.

Applying a similar idea using the gradient flow [10], we also calculate the renormalized chiral condensate in $\overline{\text{MS}}$ scheme. Although the Wilson-type quarks violates the chiral symmetry explicitly, the gradient flow method enables us to directly evaluate the chiral condensate and its susceptibility on the lattice, without suffering from power divergences. We find that the chiral condensate starts to decrease just below $T \simeq 199$ MeV. This seems to be indicating the nearby pseudocritical temperature corresponding to the chiral restoration crossover. Accordingly, we find that the disconnected chiral susceptibility shows a clear peak around $T \simeq 199$ MeV. These results are consistent with a previous estimate of $T_{\text{pc}} \sim 190$ MeV for the chiral restoration crossover [30].

Our study was made at a single lattice spacing and with heavy u and d quarks. A definite conclusion on physical observables can be made only after taking the continuum limit with physical quark masses. To carry out the continuum extrapolation, we are planning to repeat the study at different values of a . Nevertheless, the good agreement of the equation of state with the conventional method at $N_t \gtrsim 10$ seems to be suggesting that, besides the $O(1/N_t^2)$ errors at $N_t \lesssim 8$, our lattices are already close to the continuum limit for the quantities we studied. We are thus planning to start another study just at the physical quark mass point.

ACKNOWLEDGMENTS

This work is in part supported by JSPS KAKENHI Grants No. 25800148, No. 26287040, No. 26400244, No. 26400251, No. 15K05041, and No. 16H03982, by the Large Scale Simulation Program of High Energy Accelerator Research Organization (KEK) No. 14/15-23, 15/16-T06, 15/16-T-07, 15/16-25, 16/17-05 and by Interdisciplinary Computational Science Program in CCS, University of Tsukuba. This work is in part based on Lattice QCD common code Bridge++ [41].

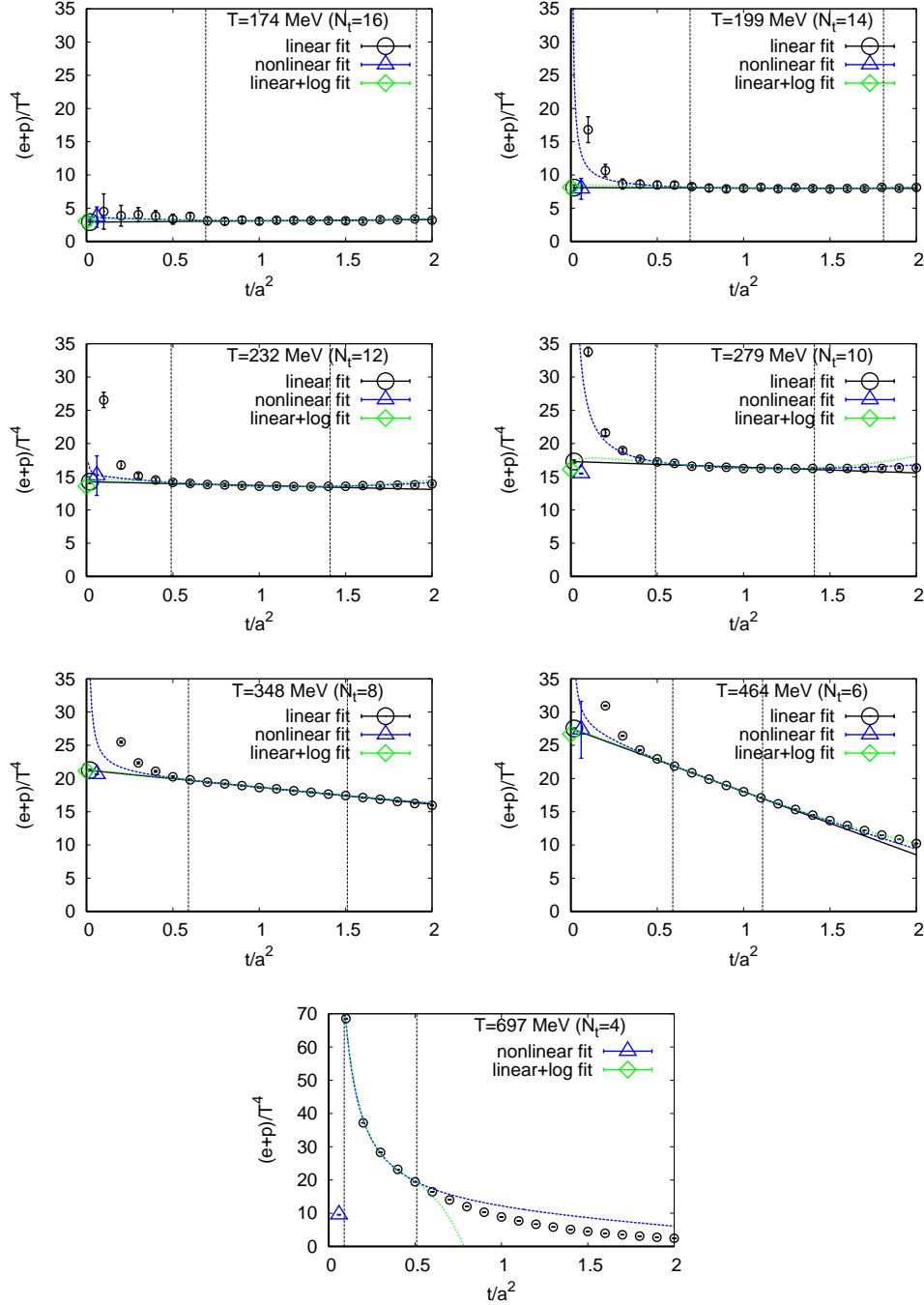


FIG. 1. Entropy density $(\epsilon + p)/T^4$ as a function of the flow time. From the top left to the bottom: $T \simeq 174, 199, 232, 279, 348, 464, 697$ MeV ($N_t = 16, 14, 12, 10, 8, 6,$ and 4 , respectively). The pair of dashed vertical lines indicates the window used for the fit at each T . Black solid lines are the fit results with the linear fit Ansatz (43), and the big open circles at $t = 0$ are the entropy density extracted from the fits. Blue and green dashed curves together with blue upward triangles and green diamonds at $t \sim 0$ are the fit results with the nonlinear Ansatz (44) and linear+log Ansatz (45), respectively. Errors are statistical only.

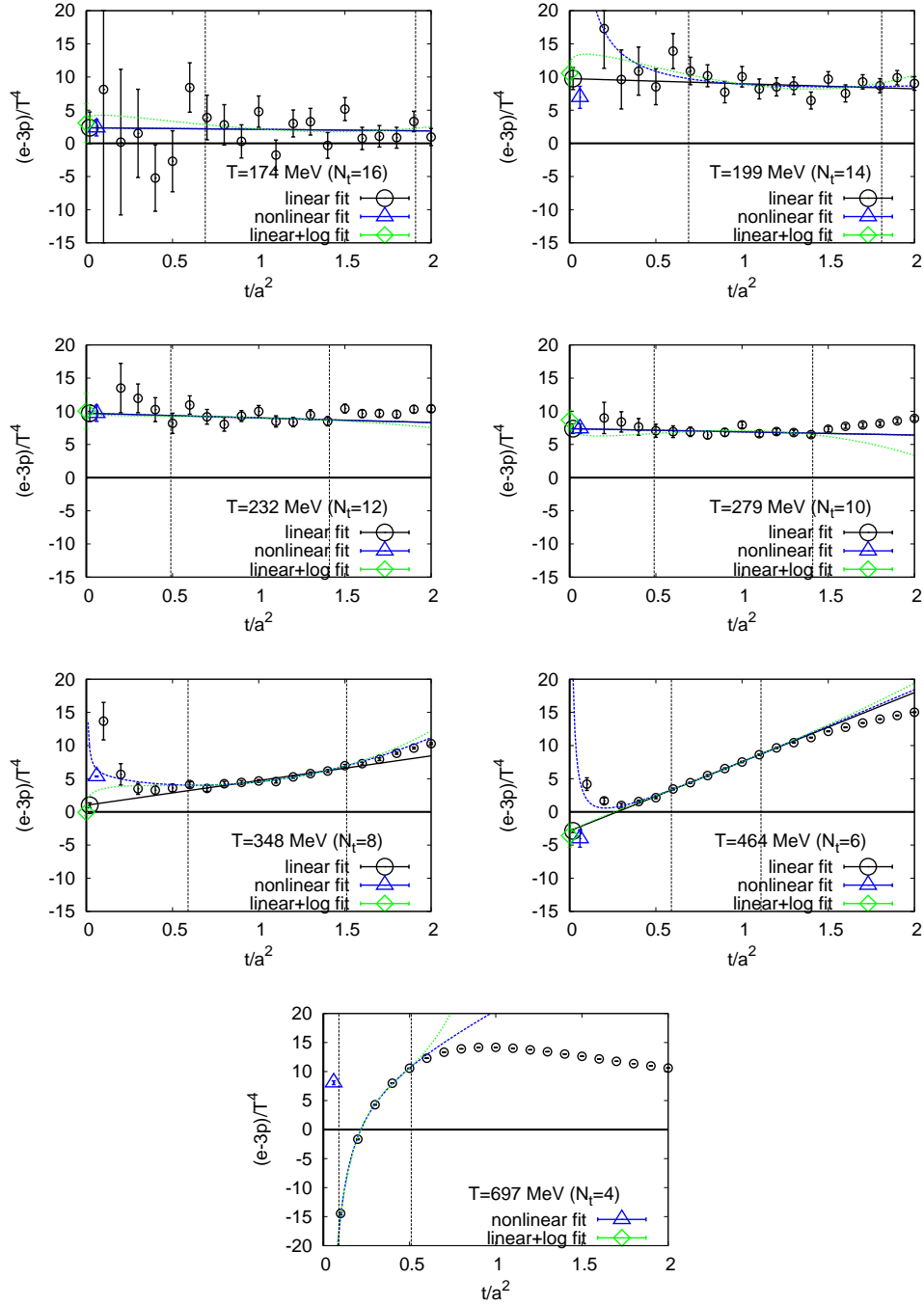


FIG. 2. The same as Fig. 1 but for the trace anomaly $(\epsilon - 3p)/T^4$.

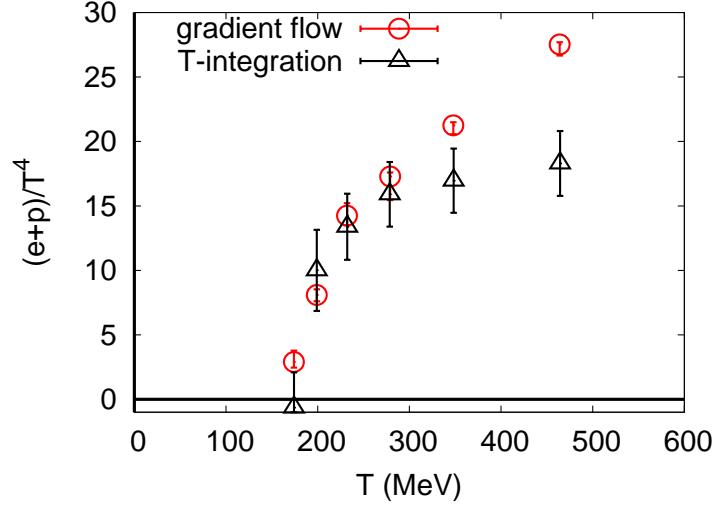


FIG. 3. Entropy density $(\epsilon + p)/T^4$ as a function of temperature. Red circles are our result with the gradient flow method. Errors include both statistical and systematic errors. Black triangles are previous results obtained by the T -integration method [30].

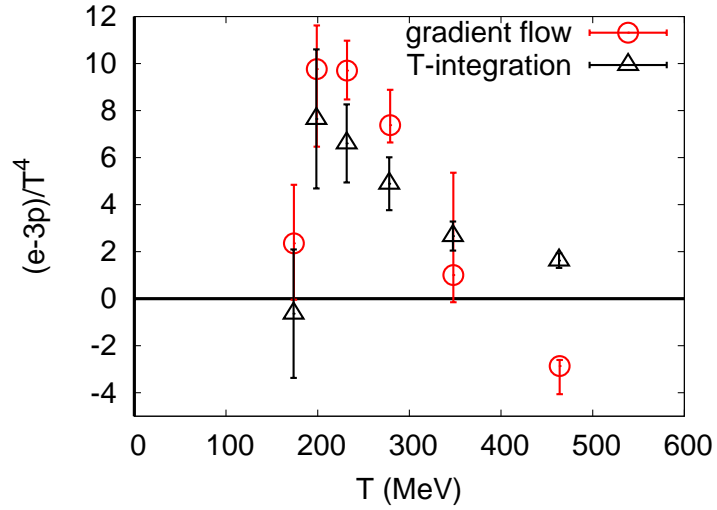


FIG. 4. The same as Fig. 3 but for the trace anomaly $(\epsilon - 3p)/T^4$.

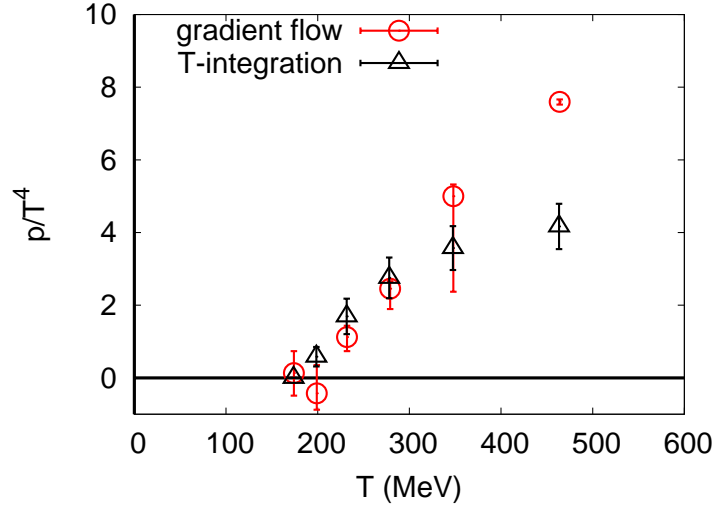


FIG. 5. The same as Fig. 3 but for the pressure p/T^4 . In the T -integration method, the pressure is set to be zero at $T \simeq 174$ MeV.

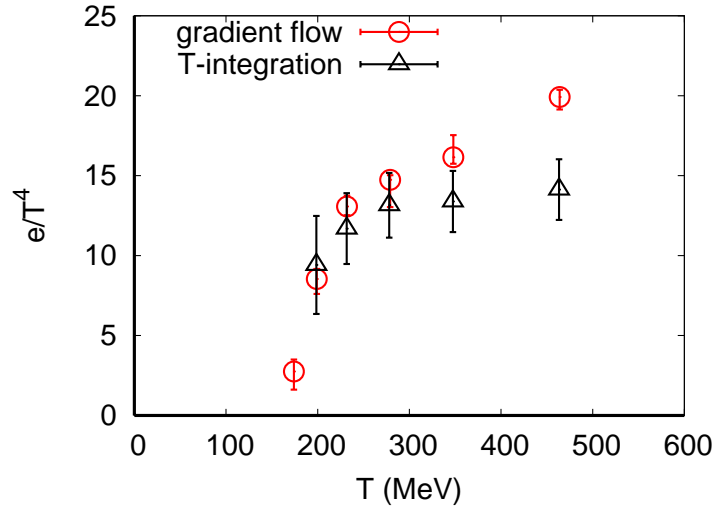


FIG. 6. The same as Fig. 3 but for the energy density ϵ/T^4 .

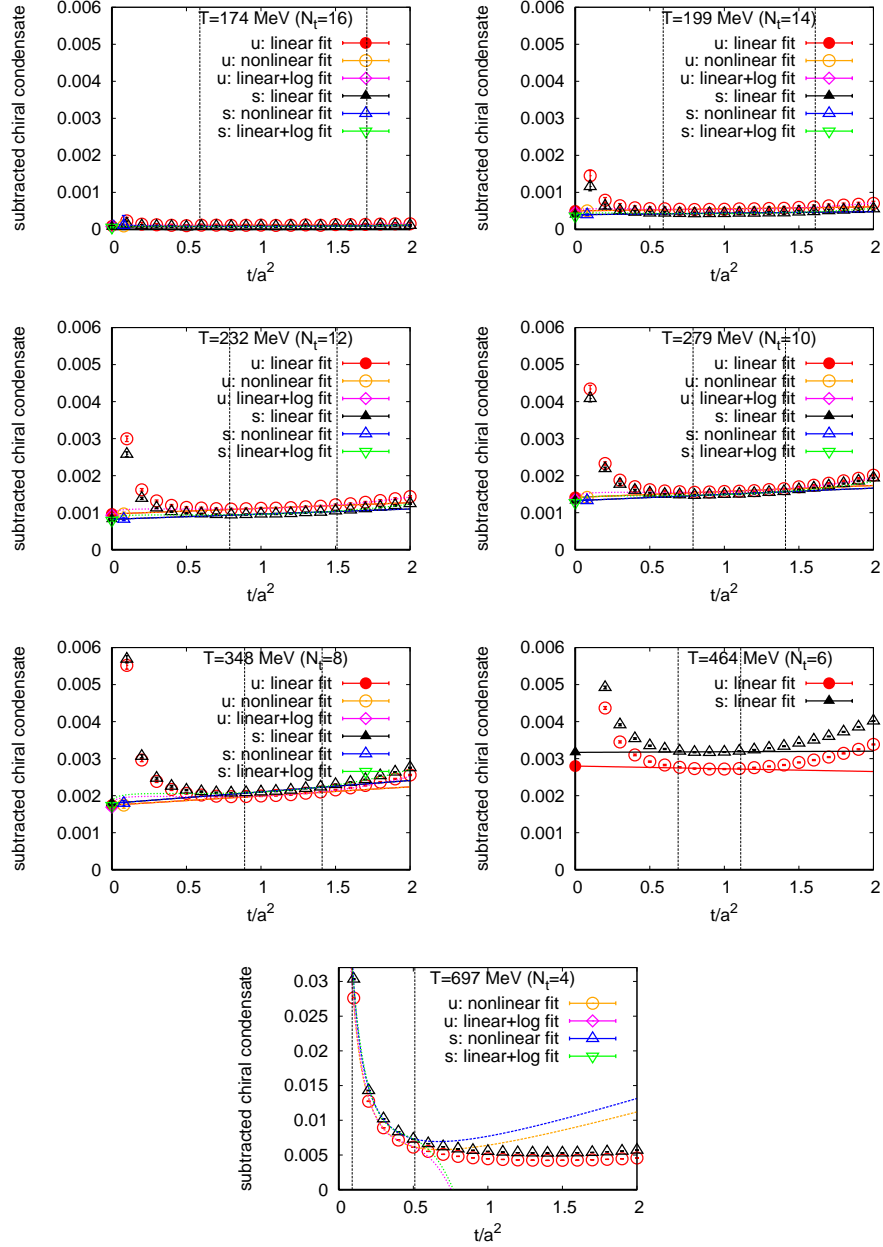


FIG. 7. Chiral condensate $\langle \{\bar{\psi}_f \psi_f\} \rangle$ with VEV subtraction as a function of the flow time. The vertical axis is in lattice unit. Red open circles and black open triangles are for $f = u$ (or d) and s , respectively. From the top left to the bottom: $T \simeq 174, 199, 232, 279, 348, 464$, and 697 MeV ($N_t = 16, 14, 12, 10, 8, 6$, and 4 , respectively). The filled symbols at $t = 0$ are the renormalized chiral condensate given by taking the $t \rightarrow 0$ limit with the linear fit. Orange and blue dashed curves with open symbols at $t \sim 0$ are the results of the nonlinear fit for u and s quark, respectively. Magenta and green dashed curves with open symbols at $t \sim 0$ are the results of the liner+log fit for u and s quark, respectively. Pair of dashed vertical lines shows the window used for the fits. Errors are statistical only.

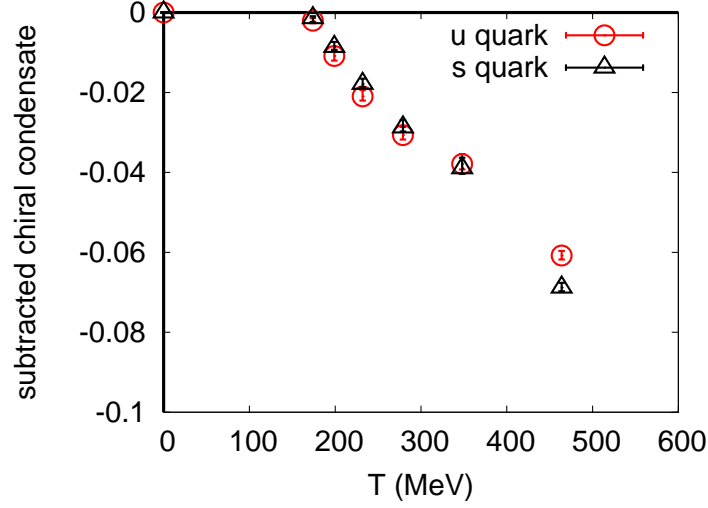


FIG. 8. Renormalized chiral condensate with the VEV subtraction, $-\langle\{\bar{\psi}_f\psi_f\}\rangle_{\overline{\text{MS}}}(\mu = 2 \text{ GeV})$, in $\overline{\text{MS}}$ scheme as a function of temperature. Following a convention, the sign is flipped in the figure. The vertical axis is in unit of GeV^3 . Red circles are u (or d) quark condensate and black triangles are that for s quark. Errors include the statistical error and the systematic error from the perturbative coefficients and fit Ansatz, except for the data at $T \simeq 464\text{MeV}$ for which the systematic error due to fit Ansatz was not estimated.

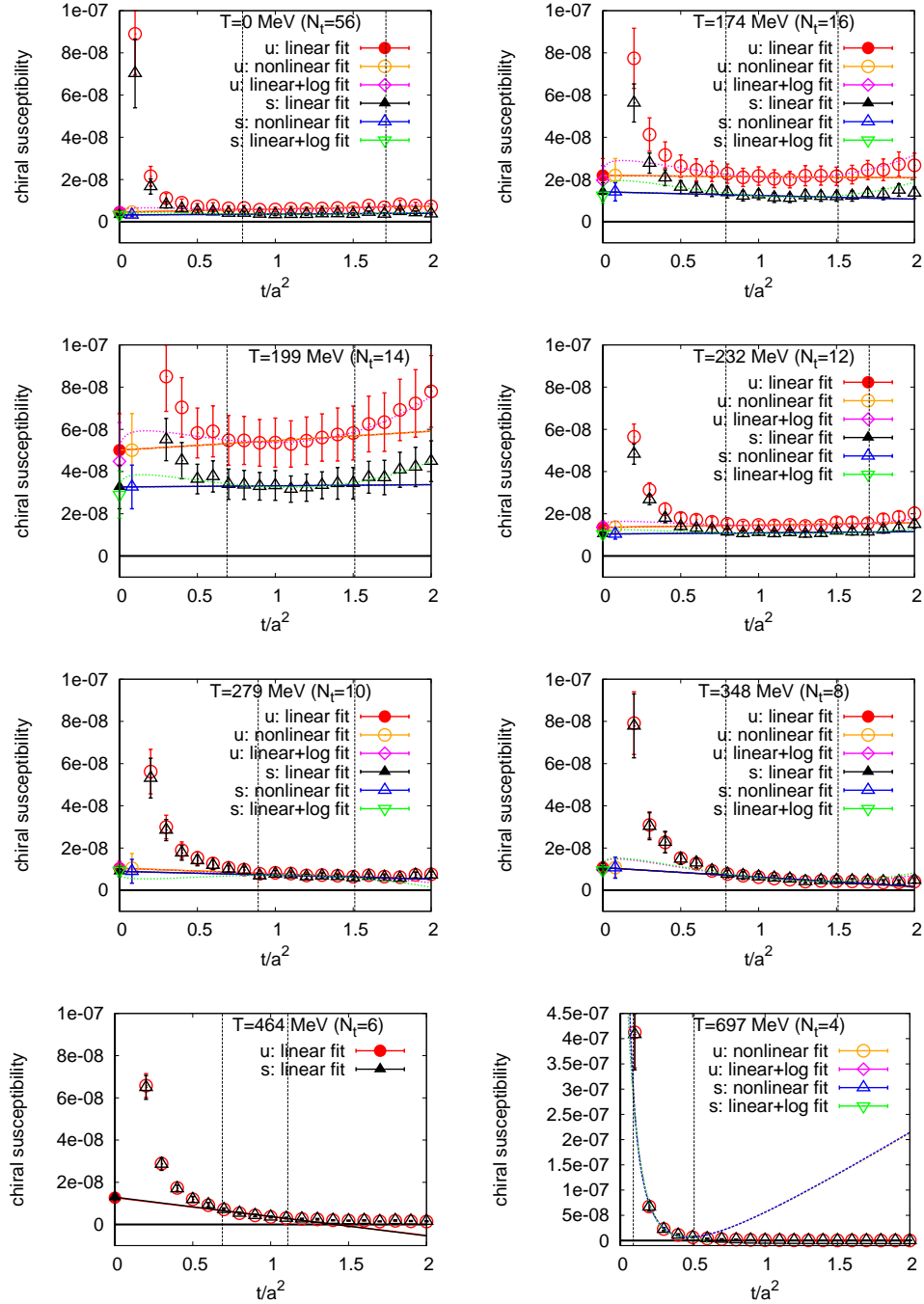


FIG. 9. The same as Fig. 7 but for the disconnected chiral susceptibility $\chi_{ff}^{\text{disc.}}$ ($\mu = 2$ GeV). From the top left to the bottom: $T \simeq 0, 174, 199, 232, 279, 348, 464,$ and 697 MeV ($N_t = 54, 16, 14, 12, 10, 8, 6,$ and $4,$ respectively).

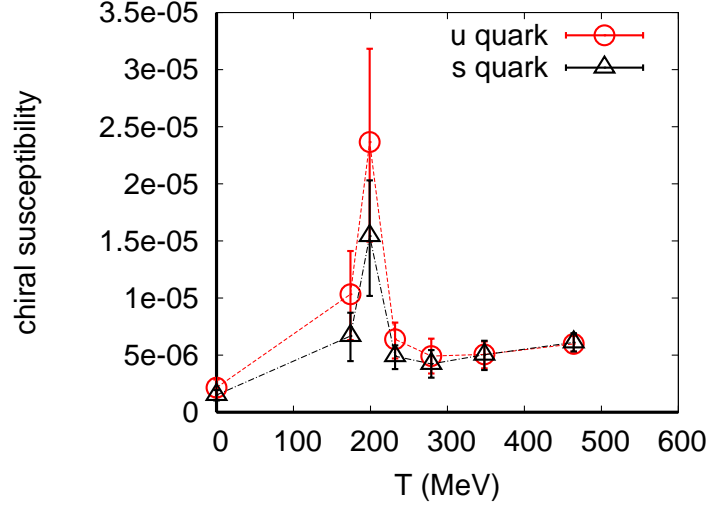


FIG. 10. Disconnected chiral susceptibility $\chi_{ff}^{\text{disc.}}(\mu = 2 \text{ GeV})$ renormalized in $\overline{\text{MS}}$ scheme as a function of temperature. The vertical axis is in unit of GeV^6 . Red circles are those of u (or d) quark and black triangles are those for s quark. Errors include the statistical error and the systematic errors from the perturbative coefficients and fit Ansatz.

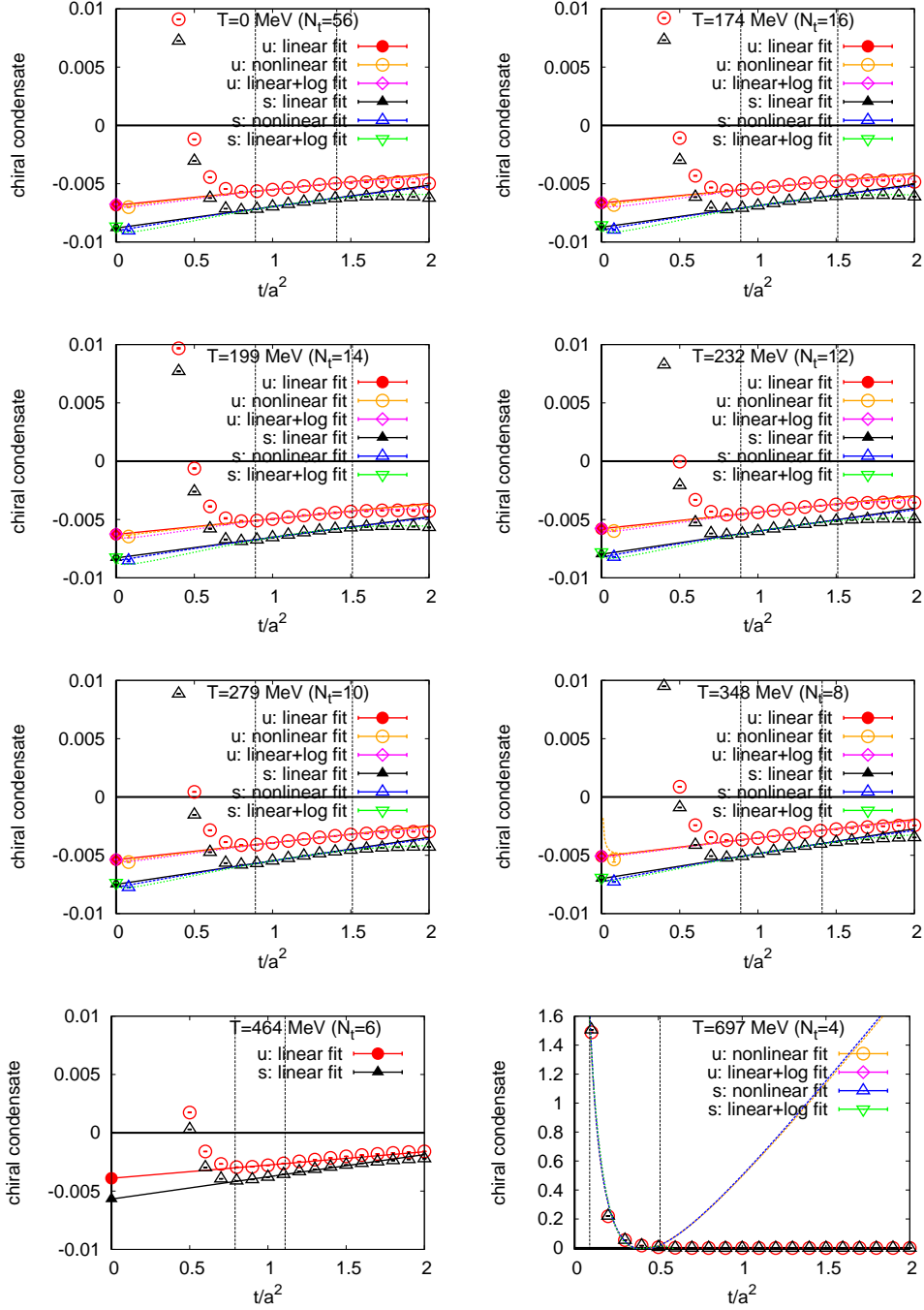


FIG. 11. The same as Fig. 7 but for the unsubtracted chiral condensate $\langle\{\bar{\psi}_f\psi_f\}^{(0)}\rangle$. From the top left to the bottom: $T \simeq 0, 174, 199, 232, 279, 348, 464,$ and 697 MeV ($N_t = 54, 16, 14, 12, 10, 8, 6,$ and $4,$ respectively).

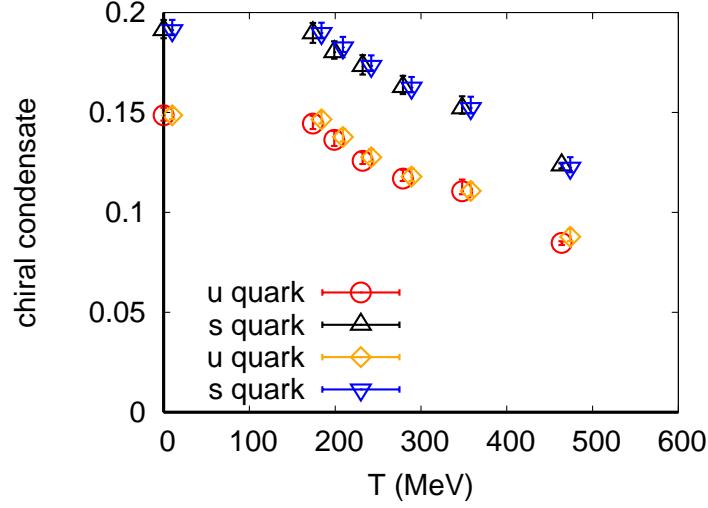


FIG. 12. Renormalized chiral condensate in $\overline{\text{MS}}$ scheme, $-\langle\{\bar{\psi}_f\psi_f\}(x)\rangle_{\overline{\text{MS}}}^{(0)}$ ($\mu = 2 \text{ GeV}$), as a function of temperature. Following a convention, the sign is flipped in the figure. The vertical axis is in unit of GeV^3 . Red circles and black upward triangles are u (or d) and s quark condensate extracted directly from the unsubtracted chiral condensate shown in Fig. 11. Orange diamonds and blue downward triangles are u and s quark condensate obtained by adding the VEV of Eqs (48) (49) to the subtracted chiral condensate shown in Fig. 8. Orange and blue symbols are slightly shifted in the horizontal direction for clarity. Errors include the statistical error and the systematic error from the perturbative coefficients and fit Ansatz, while, at $T \simeq 464 \text{ MeV}$, the systematic error due to fit Ansatz was not estimated.

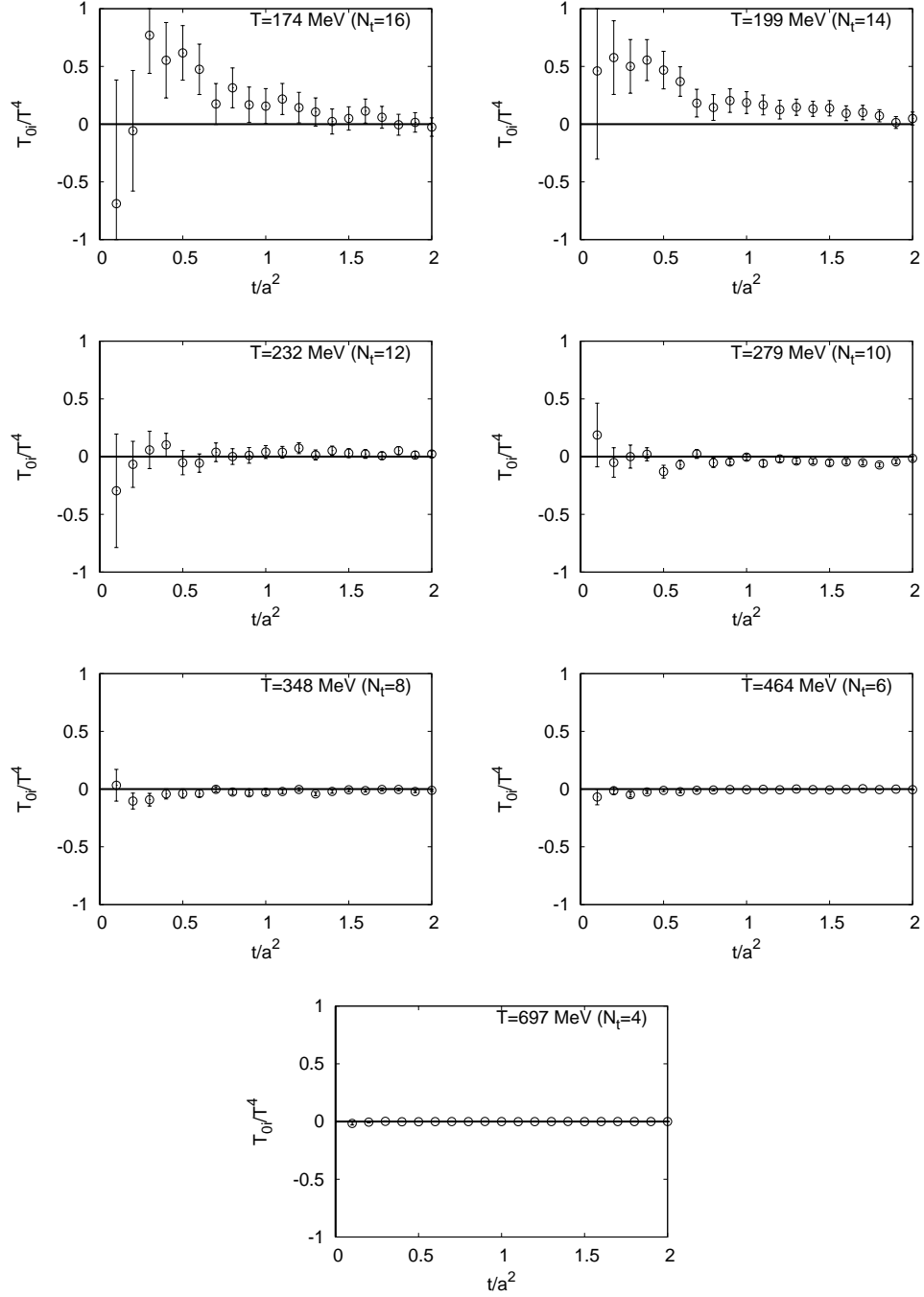


FIG. 13. Off diagonal component T_{i4}/T^4 , which corresponds to the momentum density, as a function of the flow time t/a^2 . From the top left to the bottom: $T \simeq 174, 199, 232, 279, 348, 464, 697$ MeV. Errors are statistical only.

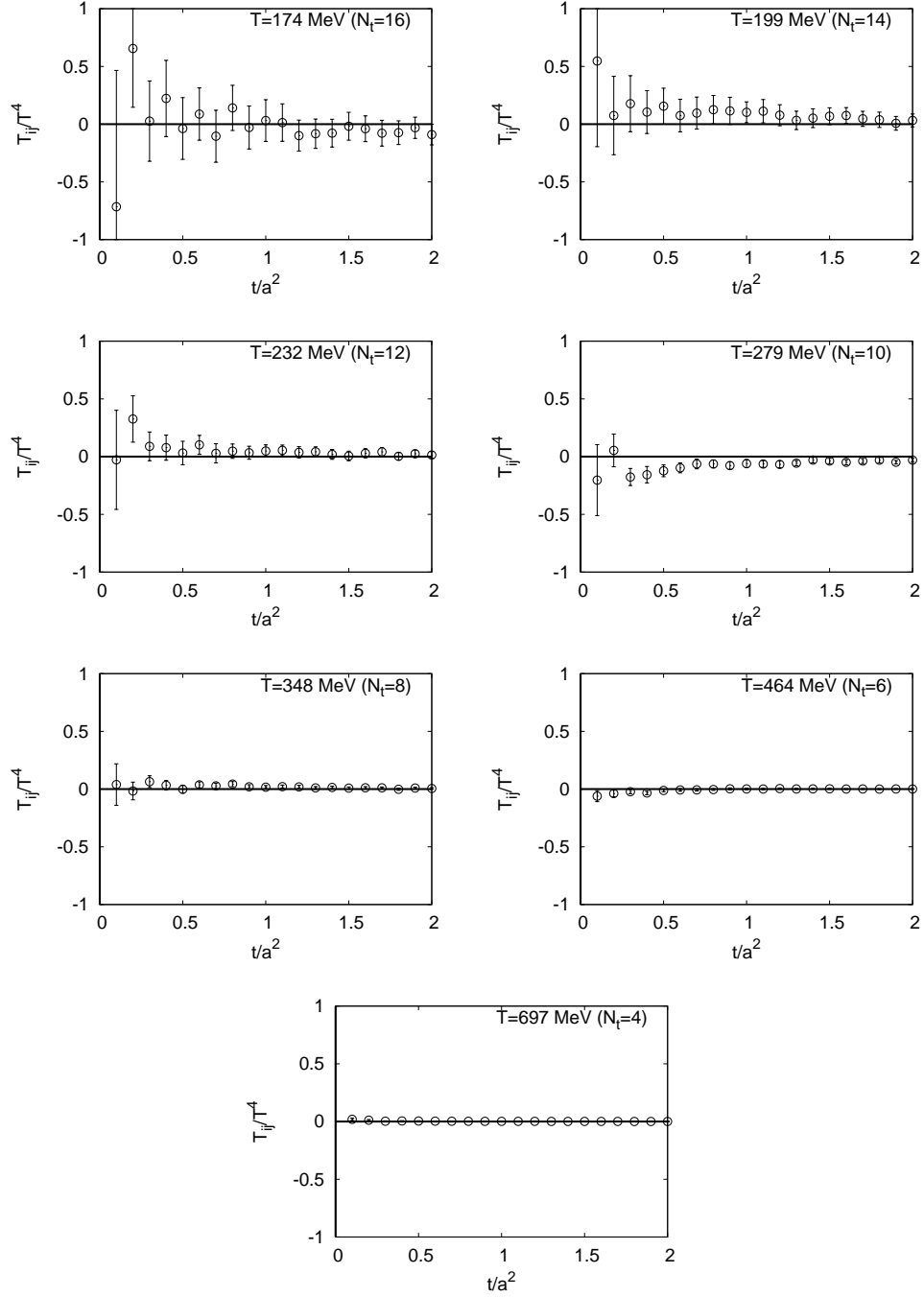


FIG. 14. The same as Fig. 13 but for the off diagonal component $T_{i \neq j}/T^4$ corresponding to the stress density.

Appendix A: Numerical algorithm for flowed quark observables

As Eqs. (11)-(13) show, to compute the thermal expectation value of the energy-momentum tensor, we need to compute expectation values,

$$t_{\mu\nu}^f(t) \equiv \frac{1}{N_\Gamma} \sum_x \left\langle \bar{\chi}_f(t, x) \gamma_\mu \left(D_\nu - \overleftarrow{D}_\nu \right) \chi_f(t, x) \right\rangle, \quad (\text{A1})$$

$$s^f(t) \equiv \frac{1}{N_\Gamma} \sum_x \langle \bar{\chi}_f(t, x) \chi_f(t, x) \rangle, \quad (\text{A2})$$

where $N_\Gamma = \sum_x$ is the number of lattice points, both at finite and zero temperatures. Note that the covariant derivatives in Eq. (A1) refer to the flowed gauge field $B_\mu(t, x)$ at the flow time t .

The basic contraction of flowed quark fields is given by [see Eq. (6.8) of Ref. [4]],

$$\overline{\chi_f(t, x) \chi_{f'}(s, y)} = \delta_{ff'} \sum_{v, w} K(t, x; 0, v) [S_f(v, w) - c_{\text{fl}} \delta_{v, w}] K(s, y; 0, w)^\dagger, \quad (\text{A3})$$

where $S_f(x, y)$ is the quark propagator with the bare mass m_{f0} ,

$$(\not{D} + m_{f0}) S_f(x, y) = \delta_{x, y}, \quad (\text{A4})$$

and $K(t, x; s, y)$ is the fundamental solution to the flow equation, defined by

$$(\partial_t - \Delta) K(t, x; s, y) = 0, \quad K(t, x; t, y) = \delta_{x, y}, \quad (\text{A5})$$

and c_{fl} is an improvement coefficient associated with the flowed quark field [4]. In Eq. (A3) and in what follows, the dagger (\dagger) implies the hermitian conjugation with respect to the gauge and spinor indices only.

Carrying out the above contraction in Eqs. (A1) and (A2), we have

$$t_{\mu\nu}^f(t) = -\frac{1}{N_\Gamma} \sum_{x, y, v, w} \left\{ \left\langle \sum_{\alpha, i} [\gamma_\mu D_\nu^x K(t, x; 0, v) S_f(v, w) K(t, y; 0, w)^\dagger]_{\alpha i, \alpha i} \delta_{y, x} \right\rangle - \left\langle \delta_{x, y} \sum_{\alpha, i} [K(t, y; 0, v) S_f(v, w) K(t, x; 0, w)^\dagger \overleftarrow{D}_\nu^x \gamma_\mu]_{\alpha i, \alpha i} \right\rangle \right\}, \quad (\text{A6})$$

$$s^f(t) = -\frac{1}{N_\Gamma} \sum_{x, y, v, w} \left\langle \sum_{\alpha, i} \{ K(t, x; 0, v) [S_f(v, w) - c_{\text{fl}} \delta_{v, w}] K(t, y; 0, w)^\dagger \}_{\alpha i, \alpha i} \delta_{y, x} \right\rangle, \quad (\text{A7})$$

where α denotes the spinor index which runs over 1, 2, 3, and 4, and i denotes the color index running over 1, 2, and 3. In writing down Eq. (A6), we have used the fact that the term in Eq. (A3) with the improvement coefficient c_{fl} does not contribute, because the trace of a single gamma matrix vanishes. Note that K and D_ν have no spinor indices.

We evaluate the above trace over space-time points stochastically (i.e., by the noise estimator). That is, we introduce a randomly generated complex scalar field $\eta(x)$ (noise field) which fulfills

$$\langle \eta(x) \rangle_\eta = 0, \quad \langle \eta(x) \eta(y)^* \rangle_\eta = \delta_{x,y}, \quad (\text{A8})$$

where expectation values refer to the average over $\eta(x)$. Then the above traces can be expressed as

$$t_{\mu\nu}^f(t) = -\frac{1}{N_\Gamma} \left\{ \left\langle \left\langle \sum_{\alpha,i} \left[\sum_{v,w} \xi(t;0,v)^\dagger S_f(v,w) \psi_{\mu\nu}(t;0,w) \right]_{\alpha i, \alpha i} \right\rangle_\eta \right\rangle - \left\langle \left\langle \sum_{\alpha,i} \left[\sum_{v,w} \psi_{\mu\nu}(t;0,v)^\dagger S_f(v,w) \xi(t;0,w) \right]_{\alpha i, \alpha i} \right\rangle_\eta \right\rangle \right\}, \quad (\text{A9})$$

$$s^f(t) = -\frac{1}{N_\Gamma} \left\langle \left\langle \sum_{\alpha,i} \left\{ \sum_{v,w} \xi(t;0,v)^\dagger [S_f(v,w) - c_{\text{fl}} \delta_{v,w}] \xi(t;0,w) \right\}_{\alpha i, \alpha i} \right\rangle_\eta \right\rangle. \quad (\text{A10})$$

Here, we have defined the combinations,

$$\xi(t; s, w) \equiv \sum_x K(t, x; s, w)^\dagger \eta(x), \quad (\text{A11})$$

$$\psi_{\mu\nu}(t; s, w) \equiv \gamma_\mu \sum_x K(t, x; s, w)^\dagger D_\nu \eta(x). \quad (\text{A12})$$

Finally, by noting

$$S_f(v, w) = \gamma_5 S_f(w, v)^\dagger \gamma_5, \quad (\text{A13})$$

we have

$$t_{\mu\nu}^f(t) = \frac{2}{N_\Gamma} \text{Re} \left\langle \left\langle \sum_{\alpha,i} \left[\sum_v \psi_{\mu\nu}(t;0,v)^\dagger \sum_w S_f(v,w) \xi(t;0,w) \right]_{\alpha i, \alpha i} \right\rangle_\eta \right\rangle, \quad (\text{A14})$$

$$s^f(t) = -\frac{1}{N_\Gamma} \left\langle \left\langle \sum_{\alpha,i} \left[\sum_v \xi(t;0,v)^\dagger \sum_w S_f(v,w) \xi(t;0,w) \right]_{\alpha i, \alpha i} \right\rangle_\eta \right\rangle + c_{\text{fl}} \frac{1}{N_\Gamma} \left\langle \left\langle \sum_{\alpha,i} \left[\sum_v \xi(t;0,v)^\dagger \xi(t;0,v) \right]_{\alpha i, \alpha i} \right\rangle_\eta \right\rangle. \quad (\text{A15})$$

So the procedure to compute the expectation values (A1) and (A2) consists of following steps:

1. Take a gauge configuration.
2. Generate a random single component complex field $\eta(x)$ which satisfies Eq. (A8).
3. Multiply $\eta(x)$ by a unit vector whose nonzero spinor-color component is (α, i) .
4. Compute $\xi(t; 0, w)$ (A11) and $\psi_{\mu\nu}(t; 0, w)$ (A12). For this, we need to solve the following “adjoint flow equations”:

$$(\partial_s + \Delta) \xi(t; s, w) = 0, \quad \xi(t; t, w) = \eta(w), \quad (\text{A16})$$

$$(\partial_s + \Delta) \psi_{\mu\nu}(t; s, w) = 0, \quad \psi_{\mu\nu}(t; t, w) = \gamma_\mu D_\nu \eta(w), \quad (\text{A17})$$

from $s = t$ to $s = 0$ *backward* in the flow time.⁹ This is the hardest part of the computation and how to carry out this integration is described in Appendix B 2.

5. Using $\xi(t; 0, w)$ obtained above as the initial vector, compute a new vector,

$$\sum_w S_f(v, w) \xi(t; 0, w), \quad (\text{A18})$$

by one of the standard methods. In the propagator defined by Eq. (A4), the gauge field is the gauge field without any flow (i.e., original link variables).

6. Compute the following inner products:

$$\frac{2}{N_\Gamma} \text{Re} \sum_v \psi_{\mu\nu}(t; 0, v)^\dagger \sum_w S_f(v, w) \xi(t; 0, w), \quad (\text{A19})$$

$$- \frac{1}{N_\Gamma} \sum_v \xi(t; 0, v)^\dagger \sum_w S_f(v, w) \xi(t; 0, w), \quad (\text{A20})$$

$$\frac{1}{N_\Gamma} \sum_v \xi(t; 0, v)^\dagger \xi(t; 0, v). \quad (\text{A21})$$

7. Change (α, i) and go back to the step (3) and repeat the above procedures for 4×3 times.

⁹ Since Δ is the unit matrix in spinor space, we can avoid the reputation of this integration over spinor indices.

8. Go back to the step (2) and repeat the above procedures for enough numbers of random fields.
9. Take a different gauge configuration and repeat the above procedures for obtaining the Monte Carlo average.

Appendix B: Numerical algorithm for gradient flow

1. Runge-Kutta integration for the gauge fields

The Wilson flow of the lattice gauge field $U(x, \mu)$ is defined by

$$(\partial_t V(t, x, \mu)) V(t, x, \mu)^{-1} = -g_0^2 \partial_{x, \mu} S_w(V), \quad V(t=0, x, \mu) = U(x, \mu), \quad (\text{B1})$$

where S_w is the Wilson plaquette action and

$$\partial_{x, \mu}^a f(U) = \left. \frac{d}{ds} f(e^{sX} U) \right|_{s=0}, \quad X(y, \nu) = \begin{cases} T^a & \text{if } (y, \nu) = (x, \mu), \\ 0 & \text{otherwise,} \end{cases} \quad (\text{B2})$$

and

$$\partial_{x, \mu} f(U) = T^a \quad \partial_{x, \mu}^a f(U). \quad (\text{B3})$$

It is convenient to write the flow equation (B1) in the following abstract form:

$$\partial_t V_t = Z(V_t) V_t. \quad (\text{B4})$$

Then the third order Runge-Kutta integration which constructs $V_{t+\epsilon}$ from V_t proceeds as follows [2]:

$$\begin{aligned} W_0 &= V_t, \\ W_1 &= \exp\left(\frac{1}{4} Z_0\right) W_0, \\ W_2 &= \exp\left(\frac{8}{9} Z_1 - \frac{17}{36} Z_0\right) W_1, \\ W_3 &= \exp\left(\frac{3}{4} Z_2 - \frac{8}{9} Z_1 + \frac{17}{36} Z_0\right) W_2, \end{aligned} \quad (\text{B5})$$

where Z_i are given from the combination defined in Eq (B4) by

$$Z_i = \epsilon Z(W_i), \quad i = 0, 1, 2, \quad (\text{B6})$$

and

$$V_{t+\epsilon} = W_3. \tag{B7}$$

With this integrator, the error in $V_{t+\epsilon}$ turns out to be $O(\epsilon^4)$.

2. Adjoint Runge-Kutta integration for the quark field

To compute the expectation value of composite operators containing flowed quark fields, we need to solve the adjoint flow equations (A16) and (A17). Since the “initial conditions” in these equations are given at the target flow time t , we have to solve the flow equations *backward* in the flow time. The equation that we want to solve can be written abstractly as

$$\partial_s \xi_s = -\Delta(V_s) \xi_s. \tag{B8}$$

Then the third order adjoint Runge-Kutta integrator that constructs ξ_s from $\xi_{s+\epsilon}$ is given by

$$\begin{aligned} \lambda_3 &= \xi_{s+\epsilon}, \\ \lambda_2 &= \frac{3}{4} \Delta_2 \lambda_3, \\ \lambda_1 &= \lambda_3 + \frac{8}{9} \Delta_1 \lambda_2, \\ \lambda_0 &= \lambda_1 + \lambda_2 + \frac{1}{4} \Delta_0 \left(\lambda_1 - \frac{8}{9} \lambda_2 \right), \end{aligned} \tag{B9}$$

where

$$\Delta_i = \epsilon \Delta(W_i), \quad i = 0, 1, 2, \tag{B10}$$

and

$$\xi_s = \lambda_0. \tag{B11}$$

The error in ξ_s is again $O(\epsilon^4)$. For the derivation of this procedure, see Appendix E.1 of Ref. [4].

In Ref. [4], the author noted that the time direction to which the Runge-Kutta integrator proceeds is quite important: One should use the Runge-Kutta steps as indicated as above but not the reversed direction, because the reversed direction is exponentially unstable. Thus, to carry out the adjoint Runge-Kutta steps (B9) from t to $t - \epsilon$, we have to compute Runge-Kutta steps for the gauge field from 0 to t . Then, for the next adjoint Runge-Kutta

step from $t - \epsilon$ to $t - 2\epsilon$, if we do not keep *any* intermediate flowed gauge-field configuration, we have to evolve the gauge field anew from 0 to $t - \epsilon$. In this way, to integrate Eqs. (A16) and (A17) backward in time from $s = t$ to $s = 0$, we have to compute the flowed gauge field from the zero flow time to intermediate flow times repeatedly. This large computational burden for the adjoint Runge-Kutta calculations can be reduced by storing intermediate flowed configurations, at the cost of the memory space.

Appendix C: Running coupling and running masses

To use the coefficients (17)–(21), we need to have the running coupling $\bar{g}(1/\sqrt{8t})$ and the running masses $\bar{m}_f(1/\sqrt{8t})$.

The renormalization group invariant scale (the Lambda parameter) is defined by

$$\frac{\Lambda}{\mu} = [b_0 \bar{g}(\mu)^2]^{-b_1/(2b_0^2)} \exp \left[-\frac{1}{2b_0 \bar{g}(\mu)^2} \right] \exp \left\{ -\int_0^{\bar{g}(\mu)} dg \left[\frac{1}{\beta(g)} + \frac{1}{b_0 g^3} - \frac{b_1}{b_0^2 g} \right] \right\}, \quad (\text{C1})$$

where μ is the renormalization scale, while the running mass and the renormalization group invariant mass M are related by

$$\bar{m}(\mu) = M [2b_0 \bar{g}(\mu)^2]^{d_0/(2b_0)} \exp \left\{ \int_0^{\bar{g}(\mu)} dg \left[\frac{\tau(g)}{\beta(g)} - \frac{d_0}{b_0 g} \right] \right\}. \quad (\text{C2})$$

The renormalization group functions, $\beta(g)$ and $\tau(g)$, are known to the four-loop order in the MS or $\overline{\text{MS}}$ scheme [42]. For the $SU(N)$ gauge theory with N_f fundamental fermions, setting

$$\beta(g) = -g^3 \sum_{k=0}^{\infty} b_k g^{2k}, \quad \tau(g) = -g^2 \sum_{k=0}^{\infty} d_k g^{2k}, \quad (\text{C3})$$

the first two coefficients are given by [43, 44]

$$b_0 = (4\pi)^{-2} \left(\frac{11}{3}N - \frac{2}{3}N_f \right), \quad (\text{C4})$$

$$b_1 = (4\pi)^{-4} \left[\frac{34}{3}N^2 - \left(\frac{13}{3}N - N^{-1} \right) N_f \right], \quad (\text{C5})$$

and [45, 46]

$$d_0 = (4\pi)^{-2} (N - N^{-1}) 3, \quad (\text{C6})$$

$$d_1 = (4\pi)^{-4} (N - N^{-1}) \left(\frac{203}{12}N - \frac{3}{4}N^{-1} - \frac{5}{3}N_f \right). \quad (\text{C7})$$

For higher orders ($k \geq 2$), setting

$$b_k = (4\pi)^{-2k-2} \sum_{l=0}^k b_{k,l} N_f^l, \quad d_k = (4\pi)^{-2k-2} (N - N^{-1}) \sum_{l=0}^k d_{k,l} N_f^l, \quad (\text{C8})$$

we have [47–49]

$$b_{2,0} = \frac{2857}{54} N^3, \quad (\text{C9})$$

$$b_{2,1} = -\frac{1709}{54} N^2 + \frac{187}{36} + \frac{1}{4} N^{-2}, \quad (\text{C10})$$

$$b_{2,2} = \frac{56}{27} N - \frac{11}{18} N^{-1}, \quad (\text{C11})$$

$$b_{3,0} = \frac{150473}{486} N^4 - \frac{40}{3} N^2 + \frac{44}{9} \zeta(3) N^4 + 352 \zeta(3) N^2, \quad (\text{C12})$$

$$b_{3,1} = -\frac{485513}{1944} N^3 + \frac{58583}{1944} N - \frac{2341}{216} N^{-1} - \frac{23}{8} N^{-3} \\ - \frac{20}{9} \zeta(3) N^3 - \frac{548}{9} \zeta(3) N + \frac{44}{9} \zeta(3) N^{-1}, \quad (\text{C13})$$

$$b_{3,2} = \frac{8654}{243} N^2 - \frac{2477}{243} - \frac{623}{54} N^{-2} + \frac{28}{3} \zeta(3) N^2 - \frac{64}{9} \zeta(3) + \frac{244}{9} \zeta(3) N^{-2}, \quad (\text{C14})$$

$$b_{3,3} = \frac{130}{243} N - \frac{77}{243} N^{-1}, \quad (\text{C15})$$

and [50–53]

$$d_{2,0} = \frac{11413}{108} N^2 - \frac{129}{8} + \frac{129}{8} N^{-2}, \quad (\text{C16})$$

$$d_{2,1} = -\frac{1177}{54} N + \frac{23}{2} N^{-1} - 12 \zeta(3) N - 12 \zeta(3) N^{-1}, \quad (\text{C17})$$

$$d_{2,2} = -\frac{35}{27}, \quad (\text{C18})$$

$$d_{3,0} = \frac{460151}{576} N^3 - \frac{66577}{576} N + \frac{50047}{192} N^{-1} + \frac{1261}{64} N^{-3} \\ + \frac{1157}{9} \zeta(3) N^3 + 104 \zeta(3) N - 47 \zeta(3) N^{-1} + 42 \zeta(3) N^{-3} \\ - 220 \zeta(5) N^3 - 220 \zeta(5) N, \quad (\text{C19})$$

$$d_{3,1} = -\frac{23816}{81} N^2 + \frac{10475}{108} + \frac{37}{3} N^{-2} \\ - \frac{889}{3} \zeta(3) N^2 - 170 \zeta(3) - 111 \zeta(3) N^{-2} + 66 \zeta(4) N^2 + 66 \zeta(4) \\ + 160 \zeta(5) N^2 + 100 \zeta(5) - 60 \zeta(5) N^{-2}, \quad (\text{C20})$$

$$d_{3,2} = \frac{899}{162} N - \frac{38}{27} N^{-1} + 20 \zeta(3) N + 20 \zeta(3) N^{-1} - 12 \zeta(4) N - 12 \zeta(4) N^{-1}, \quad (\text{C21})$$

$$d_{3,3} = -\frac{83}{81} + \frac{16}{9} \zeta(3). \quad (\text{C22})$$

For $N = 3$ and $N_f = 3$, we have

$$b_0 = (4\pi)^{-2}9, \quad (\text{C23})$$

$$b_1 = (4\pi)^{-4}64, \quad (\text{C24})$$

$$b_2 = (4\pi)^{-6}\frac{3863}{6}, \quad (\text{C25})$$

$$b_3 = (4\pi)^{-8}\left[3560\zeta(3) + \frac{140599}{18}\right], \quad (\text{C26})$$

and

$$d_0 = (4\pi)^{-2}8, \quad (\text{C27})$$

$$d_1 = (4\pi)^{-4}\frac{364}{3}, \quad (\text{C28})$$

$$d_2 = (4\pi)^{-6}\left[\frac{17770}{9} - 320\zeta(3)\right], \quad (\text{C29})$$

$$d_3 = (4\pi)^{-8}\left[-\frac{297440}{27}\zeta(3) - \frac{16000}{3}\zeta(5) + 48\pi^4 + \frac{2977517}{81}\right]. \quad (\text{C30})$$

Now, for our application, we adopt the $\overline{\text{MS}}$ scheme and set $\mu = 1/\sqrt{8t}$. Then, the left-hand side of Eq. (C1) reads

$$a\Lambda_{\overline{\text{MS}}}\sqrt{8t/a^2}. \quad (\text{C31})$$

Then by solving Eq. (C1) with respect to $\bar{g}(\mu)$ numerically, we have the running coupling $\bar{g}(1/\sqrt{8t})$ in the $\overline{\text{MS}}$ scheme. Another option (although we do not use it in the present paper) is an approximate formula quoted in the Particle Data Group [40],

$$\bar{g}(\mu)^2 = \frac{1}{b_0 t} \left[1 - \frac{b_1 \ln t}{b_0^2 t} + \frac{b_1^2 (\ln^2 t - \ln t - 1) + b_0 b_2}{b_0^4 t^2} - \frac{b_1^3 (\ln^3 t - \frac{5}{2} \ln^2 t - 2 \ln t + \frac{1}{2}) + 3b_0 b_1 b_2 \ln t - \frac{1}{2} b_0^2 b_3}{b_0^6 t^3} \right], \quad t \equiv \ln \left(\frac{\mu^2}{\Lambda^2} \right). \quad (\text{C32})$$

For $\Lambda_{\overline{\text{MS}}}$, we use the value [40],

$$\Lambda_{\overline{\text{MS}}}^{(3)} = 332(19) \text{ MeV}. \quad (\text{C33})$$

Using [31]

$$a(\beta = 2.05) = 0.0701(29) \text{ fm}, \quad (\text{C34})$$

we have

$$a(\beta = 2.05) \Lambda_{\overline{\text{MS}}} = 0.0701(29) \times 332(19)/197.3269718. \quad (\text{C35})$$

For the renormalization group invariant mass, we adopt [31, 54],

$$\begin{aligned} a(\beta = 2.05) M &= Z_m(\beta = 2.05) a(\beta = 2.05) m_{u,d} \\ &= 1.862(41) \times (0.02105 \pm 0.00017), \end{aligned} \quad (\text{C36})$$

for u and d quarks, and

$$\begin{aligned} a(\beta = 2.05) M &= Z_m(\beta = 2.05) a(\beta = 2.05) m_s \\ &= 1.862(41) \times (0.03524 \pm 0.00026), \end{aligned} \quad (\text{C37})$$

for s quark. Then the running masses $a\bar{m}_{ud}(1/\sqrt{8t})$ and $a\bar{m}_s(1/\sqrt{8t})$ are given by Eq. (C2).

Appendix D: Additional tests on the energy-momentum tensor

In this Appendix, we summarize our additional tests on our results of the energy-momentum tensor discussed in Sec. IV.

1. Off diagonal components

In order to check validity of the formulation, we calculate off diagonal components of the energy-momentum tensor. In Fig. 13 and 14, we plot the off diagonal components T_{i4}/T^4 and $T_{i\neq j}/T^4$, which correspond to the momentum and stress density, respectively, as functions of t/a^2 .

We first confirm that the data are consistent with zero within 2σ in the fit windows adopted in Sec. IV A. By identifying windows for the linear fit for each data, we find that the $t \rightarrow 0$ extrapolation sometimes leads to a value which is slightly off the 0. However, because the tendency as a function of T is not uniform, we consider that this is caused by an accidental fluctuation due to insufficient statistics or an optimistic error estimation disregarding the correlation in t/a^2 .

2. Gauge and quark contributions

One may interested in how the gauge and quark operators contribute to the energy-momentum tensor quantitatively. In Figs. 15 and 16, the entropy density and trace anomaly

are plotted as a function of the flow time t/a^2 , respectively. In these figures, we break up contributions from gauge operators (9) and (10) and those from quark operators (11), (12) and (13) from ud and s quarks, where the ud quark contribution is a mixture of those from u and d quark.

In general, the magnitude of contributions from the gauge and each quarks are almost the same for the energy and entropy density. The trace anomaly is dominated by the gauge contribution at $T \simeq 200\text{-}350$ MeV. On the other hand, the quarks dominate at higher temperatures, which however is suspected to be contaminated by a lattice artifact. For the pressure, gauge and quark contributions are similar in magnitude but opposite in sign at low temperatures. At high temperatures, the quark contributions dominates but is also suspected to be contaminated by a lattice artifact.

We note that the singular behavior a^2/t in the equation of state close to the origin comes dominantly from the quark operators.

3. Lattice operators for the field strength

For the quadratic terms of the field strength tensor $G_{\mu\nu}(x)$ in Eqs. (9) and (10), there are several alternative choices of lattice operators. In this study, we construct clover operators with four plaquette Wilson loops and with eight 1×2 rectangle Wilson loops. Combining these two clover operators, we get the tree-level improved field strength squared [38].

We also test a definition using the imaginary part of a plaquette Wilson loop. In summary, we study the following four alternatives [55]:

- (i) the tree-level improved operator given by combining two clover term contributions with four plaquette and eight 1×2 rectangle Wilson loops,
- (ii) the clover term with four plaquette Wilson loops,
- (iii) the clover term with eight 1×2 rectangle Wilson loops,
- (iv) the imaginary part of the plaquette Wilson loop.

We adopt the first combination for the central value of our estimations and estimate a part of the $O(a^2)$ lattice artifacts in the gauge operator by comparing the results of four alternatives.

In Figs. 17 and 18, we plot the entropy density and trace anomaly as functions of temperature by changing the operator for the field strength squared. We confirm that the results are consistent with each other, while that with the clover term with eight 1×2 rectangles shows slight deviation. This may be because the $O(a^2)$ lattice artifact is severer for that definition. Disregarding the data at $T \simeq 697$ MeV ($N_t = 4$), we conclude that the systematic error from the choice of the operators for the gauge contribution is small.

-
- [1] M. Lüscher, “Trivializing maps, the Wilson flow and the HMC algorithm,” *Commun. Math. Phys.* **293**, 899 (2010) doi:10.1007/s00220-009-0953-7 [arXiv:0907.5491 [hep-lat]].
 - [2] M. Lüscher, “Properties and uses of the Wilson flow in lattice QCD,” *J. High Energy Phys.* **1008**, 071 (2010) Erratum: [*J. High Energy Phys.* **1403**, 092 (2014)] doi:10.1007/JHEP08(2010)071, 10.1007/JHEP03(2014)092 [arXiv:1006.4518 [hep-lat]].
 - [3] M. Lüscher and P. Weisz, “Perturbative analysis of the gradient flow in nonabelian gauge theories,” *J. High Energy Phys.* **1102**, 051 (2011) doi:10.1007/JHEP02(2011)051 [arXiv:1101.0963 [hep-th]].
 - [4] M. Lüscher, “Chiral symmetry and the Yang-Mills gradient flow,” *J. High Energy Phys.* **1304**, 123 (2013) doi:10.1007/JHEP04(2013)123 [arXiv:1302.5246 [hep-lat]].
 - [5] R. Narayanan and H. Neuberger, “Infinite N phase transitions in continuum Wilson loop operators,” *J. High Energy Phys.* **0603**, 064 (2006) doi:10.1088/1126-6708/2006/03/064 [hep-th/0601210].
 - [6] M. Lüscher, “Future applications of the Yang-Mills gradient flow in lattice QCD,” *Proc. Sci. LATTICE* **2013**, 016 (2014) [arXiv:1308.5598 [hep-lat]].
 - [7] A. Ramos, “The Yang-Mills gradient flow and renormalization,” *Proc. Sci. LATTICE* **2014**, 017 (2015) [arXiv:1506.00118 [hep-lat]].
 - [8] H. Suzuki, “Energy-momentum tensor on the lattice: recent developments,” *Proc. Sci. LATTICE* **2016**, 002 (2017) [arXiv:1612.00210 [hep-lat]].
 - [9] H. Makino and H. Suzuki, “Lattice energy-momentum tensor from the Yang-Mills gradient flow—inclusion of fermion fields,” *Progr. Theor. Exp. Phys.* **2014**, 063B02 (2014) Erratum: [*Progr. Theor. Exp. Phys.* **2015**, 079202 (2015)] doi:10.1093/ptep/ptu070, 10.1093/ptep/ptv095 [arXiv:1403.4772 [hep-lat]].

- [10] K. Hieda and H. Suzuki, “Small flow-time representation of fermion bi-linear operators,” *Mod. Phys. Lett. A* **31**, 1650214 (2017) [arXiv:1606.04193 [hep-lat]].
- [11] S. Borsanyi, Z. Fodor, C. Hoelbling, S. D. Katz, S. Krieg and K. K. Szabo, “Full result for the QCD equation of state with 2+1 flavors,” *Phys. Lett. B* **730**, 99 (2014) doi:10.1016/j.physletb.2014.01.007 [arXiv:1309.5258 [hep-lat]].
- [12] A. Bazavov *et al.* (HotQCD Collaboration), “Equation of state in (2+1)-flavor QCD,” *Phys. Rev. D* **90**, 094503 (2014) doi:10.1103/PhysRevD.90.094503 [arXiv:1407.6387 [hep-lat]].
- [13] T. Umeda, S. Ejiri, S. Aoki, T. Hatsuda, K. Kanaya, Y. Maezawa and H. Ohno, “Fixed scale approach to equation of state in lattice QCD,” *Phys. Rev. D* **79**, 051501 (2009) doi:10.1103/PhysRevD.79.051501 [arXiv:0809.2842 [hep-lat]].
- [14] F. Burger *et al.* (tmfT Collaboration), “Equation of state of quark-gluon matter from lattice QCD with two flavors of twisted mass Wilson fermions,” *Phys. Rev. D* **91**, no. 7, 074504 (2015) doi:10.1103/PhysRevD.91.074504 [arXiv:1412.6748 [hep-lat]].
- [15] Heng-Tong Ding, “Lattice QCD at nonzero temperature and density,” *Proc. Sci. LATTICE* **2016**, 022 (2017).
- [16] H. Suzuki, “Energy-momentum tensor from the Yang-Mills gradient flow,” *Progr. Theor. Exp. Phys.* **2013**, 083B03 (2013) Erratum: [*Progr. Theor. Exp. Phys.* **2015**, 079201 (2015)] doi:10.1093/ptep/ptt059, 10.1093/ptep/ptv094 [arXiv:1304.0533 [hep-lat]].
- [17] H. Makino, F. Sugino and H. Suzuki, “Large- N limit of the gradient flow in the 2D $O(N)$ nonlinear sigma model,” *Progr. Theor. Exp. Phys.* **2015**, no. 4, 043B07 (2015) doi:10.1093/ptep/ptv044 [arXiv:1412.8218 [hep-lat]].
- [18] H. Suzuki, “Universal formula for the energy-momentum tensor via a flow equation in the Gross-Neveu model,” *Progr. Theor. Exp. Phys.* **2015**, no. 4, 043B04 (2015) doi:10.1093/ptep/ptv036 [arXiv:1501.04371 [hep-lat]].
- [19] M. Asakawa *et al.* (FlowQCD Collaboration), “Thermodynamics of $SU(3)$ gauge theory from gradient flow on the lattice,” *Phys. Rev. D* **90**, no. 1, 011501 (2014) Erratum: [*Phys. Rev. D* **92**, no. 5, 059902 (2015)] doi:10.1103/PhysRevD.90.011501, 10.1103/PhysRevD.92.059902 [arXiv:1312.7492 [hep-lat]].
- [20] G. Boyd, J. Engels, F. Karsch, E. Laermann, C. Legeland, M. Lütgemeier and B. Petersson, “Thermodynamics of $SU(3)$ lattice gauge theory,” *Nucl. Phys. B* **469**, 419 (1996)

- doi:10.1016/0550-3213(96)00170-8 [hep-lat/9602007].
- [21] M. Okamoto *et al.* (CP-PACS Collaboration), “Equation of state for pure $SU(3)$ gauge theory with renormalization group improved action,” *Phys. Rev. D* **60**, 094510 (1999) doi:10.1103/PhysRevD.60.094510 [hep-lat/9905005].
- [22] Y. Namekawa *et al.* (CP-PACS Collaboration), “Thermodynamics of $SU(3)$ gauge theory on anisotropic lattices,” *Phys. Rev. D* **64**, 074507 (2001) doi:10.1103/PhysRevD.64.074507 [hep-lat/0105012].
- [23] L. Levkova, T. Manke and R. Mawhinney, “Two-flavor QCD thermodynamics using anisotropic lattices,” *Phys. Rev. D* **73**, 074504 (2006) doi:10.1103/PhysRevD.73.074504 [hep-lat/0603031].
- [24] S. Borsányi, G. Endrődi, Z. Fodor, S. D. Katz and K. K. Szabó, “Precision $SU(3)$ lattice thermodynamics for a large temperature range,” *J. High Energy Phys.* **1207**, 056 (2012) doi:10.1007/JHEP07(2012)056 [arXiv:1204.6184 [hep-lat]].
- [25] Y. Taniguchi, K. Kanaya, H. Suzuki, and T. Umeda, “Topological susceptibility in finite temperature $(2 + 1)$ -flavor QCD using gradient flow,” *Phys. Rev. D* **95**, no. 5, 054502 (2017) doi:10.1103/PhysRevD.95.054502 [arXiv:1611.02411 [hep-lat]].
- [26] K. Kanaya, E. Ejiri, R. Iwami, M. Kitazawa, H. Suzuki, Y. Taniguchi, T. Umeda, and N. Wakabayashi, “Equation of state in $(2 + 1)$ -flavor QCD with gradient flow,” *Proc. Sci. LATTICE* **2016**, 063 (2017) [arXiv:1610.09518 [hep-lat]].
- [27] Y. Taniguchi, E. Ejiri, K. Kanaya, M. Kitazawa, H. Suzuki, T. Umeda, R. Iwami, and N. Wakabayashi, “Temperature dependence of topological susceptibility using gradient flow,” *Proc. Sci. LATTICE* **2016**, 064 (2017) [arXiv:1611.02413 [hep-lat]].
- [28] K. Hieda, H. Makino and H. Suzuki, “Proof of the renormalizability of the gradient flow,” *Nucl. Phys. B* **918**, 23 (2017) doi:10.1016/j.nuclphysb.2017.02.017 [arXiv:1604.06200 [hep-lat]].
- [29] T. Endo, K. Hieda, D. Miura and H. Suzuki, “Universal formula for the flavor nonsinglet axial-vector current from the gradient flow,” *Progr. Theor. Exp. Phys.* **2015**, no. 5, 053B03 (2015) doi:10.1093/ptep/ptv058 [arXiv:1502.01809 [hep-lat]].
- [30] T. Umeda *et al.* (WHOT-QCD Collaboration), “Equation of state in $2 + 1$ flavor QCD with improved Wilson quarks by the fixed scale approach,” *Phys. Rev. D* **85**, 094508 (2012) doi:10.1103/PhysRevD.85.094508 [arXiv:1202.4719 [hep-lat]].
- [31] T. Ishikawa *et al.* (JLQCD Collaboration), “Light quark masses from unquenched lattice

- QCD,” Phys. Rev. D **78**, 011502 (2008) doi:10.1103/PhysRevD.78.011502 [arXiv:0704.1937 [hep-lat]].
- [32] C. M. Maynard, “International Lattice Data Grid: Turn on, plug in, and download,” Proc. Sci. LATTICE**2009**, 020 (2009) [arXiv:1001.5207 [hep-lat]].
- [33] B. Sheikholeslami and R. Wohlert, “Improved continuum limit lattice action for QCD with Wilson fermions,” Nucl. Phys. B **259**, 572 (1985). doi:10.1016/0550-3213(85)90002-1
- [34] Y. Iwasaki, “Renormalization group analysis of lattice theories and improved lattice action. II. Four-dimensional non-Abelian $SU(N)$ gauge model,” arXiv:1111.7054 [hep-lat].
- [35] Y. Iwasaki, “Renormalization group analysis of lattice theories and improved lattice action: Two-dimensional nonlinear $O(N)$ sigma model,” Nucl. Phys. B **258**, 141 (1985). doi:10.1016/0550-3213(85)90606-6
- [36] Y. Maezawa *et al.* [WHOT-QCD Collaboration], “Heavy-quark free energy at finite temperature with 2 + 1 flavors of improved Wilson quarks in fixed scale approach,” Proc. Sci. LATTICE**2009**, 165 (2009) [arXiv:0911.0254 [hep-lat]].
- [37] S. Aoki *et al.* (CP-PACS and JLQCD Collaborations), “Nonperturbative $O(a)$ improvement of the Wilson quark action with the RG-improved gauge action using the Schrödinger functional method,” Phys. Rev. D **73**, 034501 (2006) doi:10.1103/PhysRevD.73.034501 [hep-lat/0508031].
- [38] A. Ali Khan *et al.* (CP-PACS Collaboration), “Topological susceptibility in lattice QCD with two flavors of dynamical quarks,” Phys. Rev. D **64**, 114501 (2001) doi:10.1103/PhysRevD.64.114501 [hep-lat/0106010].
- [39] L. Del Debbio, A. Patella and A. Rago, “Space-time symmetries and the Yang-Mills gradient flow,” J. High Energy Phys. **1311**, 212 (2013) doi:10.1007/JHEP11(2013)212 [arXiv:1306.1173 [hep-th]].
- [40] S. Bethke, G. Dissertori and G.P. Salam (Particle Data Group), Quantum Chromodynamics (2015), Chapt. 9, <http://pdg.lbl.gov/2015/reviews/rpp2015-rev-qcd.pdf>
- [41] http://bridge.kek.jp/Lattice-code/index_e.html
- [42] M. Czakon, “The four-loop QCD β -function and anomalous dimensions,” Nucl. Phys. B **710**, 485 (2005) doi:10.1016/j.nuclphysb.2005.01.012 [hep-ph/0411261].
- [43] W. E. Caswell, “Asymptotic behavior of non-abelian gauge theories to two-loop order,” Phys. Rev. Lett. **33**, 244 (1974). doi:10.1103/PhysRevLett.33.244

- [44] D. R. T. Jones, “Two-loop diagrams in Yang-Mills theory,” Nucl. Phys. B **75**, 531 (1974). doi:10.1016/0550-3213(74)90093-5
- [45] R. Tarrach, “The pole mass in perturbative QCD,” Nucl. Phys. B **183**, 384 (1981). doi:10.1016/0550-3213(81)90140-1
- [46] O. Nachtmann and W. Wetzel, “The β -function for effective quark masses to two loops in QCD,” Nucl. Phys. B **187**, 333 (1981). doi:10.1016/0550-3213(81)90278-9
- [47] O. V. Tarasov, A. A. Vladimirov and A. Y. Zharkov, “The Gell-Mann–Low function of QCD in the three-loop approximation,” Phys. Lett. B **93**, 429 (1980). doi:10.1016/0370-2693(80)90358-5
- [48] S. A. Larin and J. A. M. Vermaseren, “The three-loop QCD β -function and anomalous dimensions,” Phys. Lett. B **303**, 334 (1993) doi:10.1016/0370-2693(93)91441-O [hep-ph/9302208].
- [49] T. van Ritbergen, J. A. M. Vermaseren and S. A. Larin, “The four-loop β -function in quantum chromodynamics,” Phys. Lett. B **400**, 379 (1997) doi:10.1016/S0370-2693(97)00370-5 [hep-ph/9701390].
- [50] O. V. Tarasov, “Anomalous dimensions of quark masses in three loop approximation,” Report No. JINR-P2-82-900.
- [51] S. A. Larin, “The Renormalization of the axial anomaly in dimensional regularization,” Phys. Lett. B **303**, 113 (1993) doi:10.1016/0370-2693(93)90053-K [hep-ph/9302240].
- [52] K. G. Chetyrkin, “Quark mass anomalous dimension to $O(\alpha_s^4)$,” Phys. Lett. B **404**, 161 (1997) doi:10.1016/S0370-2693(97)00535-2 [hep-ph/9703278].
- [53] J. A. M. Vermaseren, S. A. Larin and T. van Ritbergen, “The 4-loop quark mass anomalous dimension and the invariant quark mass,” Phys. Lett. B **405**, 327 (1997) doi:10.1016/S0370-2693(97)00660-6 [hep-ph/9703284].
- [54] S. Aoki *et al.* [PACS-CS Collaboration], “Non-perturbative renormalization of quark mass in $N_f = 2 + 1$ QCD with the Schroedinger functional scheme,” J. High Energy Phys. **1008**, 101 (2010) doi:10.1007/JHEP08(2010)101 [arXiv:1006.1164 [hep-lat]].
- [55] C. Alexandrou, A. Athenodorou and K. Jansen, “Topological charge using cooling and the gradient flow,” Phys. Rev. D **92**, no. 12, 125014 (2015) doi:10.1103/PhysRevD.92.125014 [arXiv:1509.04259 [hep-lat]].

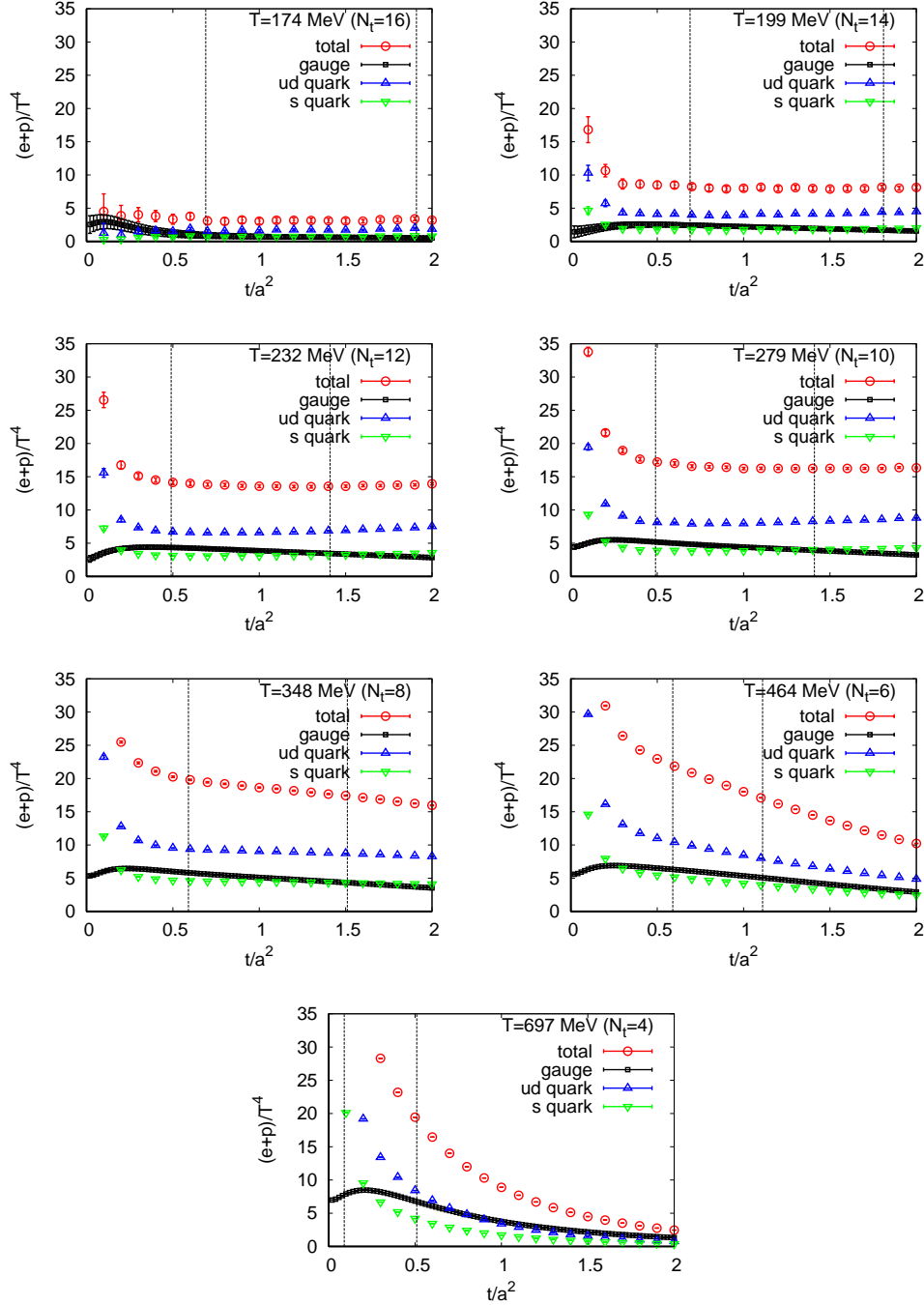


FIG. 15. Breakup of contributions from gauge and quark operators in the entropy density $(\epsilon+p)/T^4$ as a function of the flow time t/a^2 . From the top left: $T \simeq 174, 199, 232, 279, 348, 464, 697$ MeV ($N_t = 16, 14, 12, 10, 8, 6,$ and 4 , respectively). Black squares are contribution from gauge operators (9) and (10). Blue and green triangles are those from quark operators (11), (12) and (13) with ud and s quarks. Red circles are the sum of all contributions. Pair of dashed vertical lines indicates the window used for the fit.

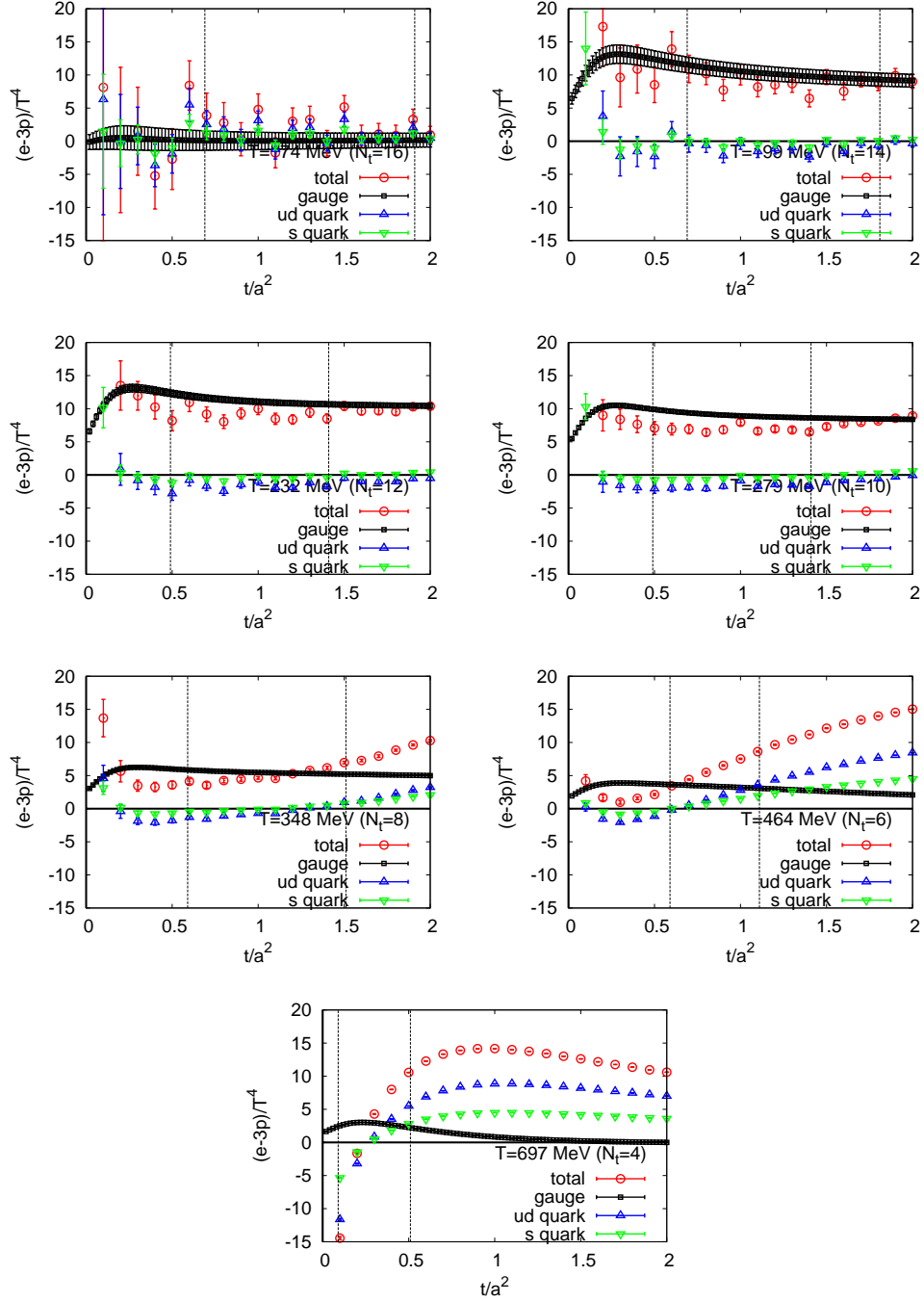


FIG. 16. The same as Fig. 15 but for the trace anomaly $(\epsilon - 3p)/T^4$.

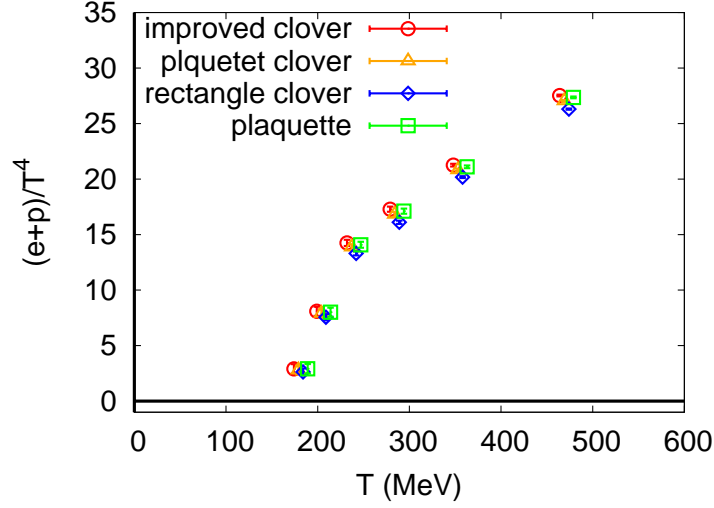


FIG. 17. Entropy density $(\epsilon + p)/T^4$ as a function of temperature adopting four different operators for the field strength squared. (i) Red circles are results where the tree level improved combination of the clover terms is used to define the field strength squared for the gauge contribution. Orange, blue, and green symbols are the results adopting (ii) the clover term with four plaquettes, (iii) the clover term with eight 1×2 rectangle Wilson loops, and (iv) the imaginary part of the plaquette to define the field strength. Symbols are slightly shifted in the horizontal direction for clarity of the figure. Errors are statistical only..

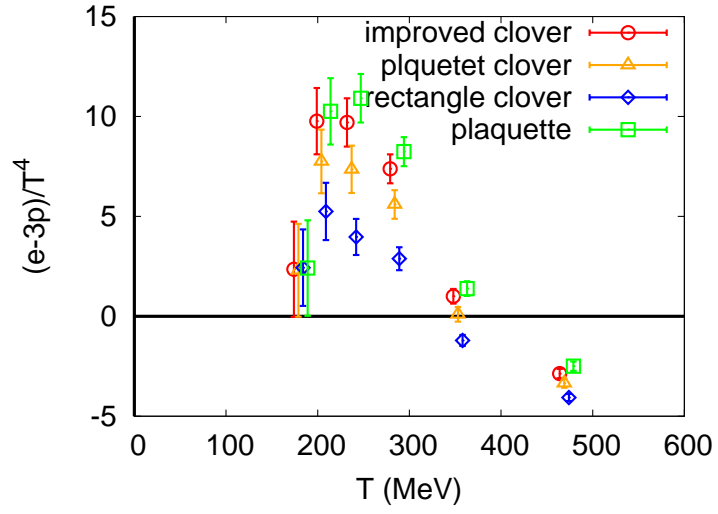


FIG. 18. The same as Fig. 17 but for the trace anomaly $(\epsilon - 3p)/T^4$.